

JAMES | Journal of Advances in Modeling Earth Systems*

RESEARCH ARTICLE

10.1029/2025MS005067

Key Points:

- Updated historical anthropogenic aerosol data for simple plumes for CMIP6plus and CMIP7 show moderate differences to the CMIP6 version
- Effective radiative forcing of anthropogenic aerosols is -0.33 Wm⁻² for 2014 in ICON XPP with little influence of its base state
- Assessed climate responses to the CMIP6 and CMIP7 data for simple plumes are similar in ensembles of ICON XPP historical experiments

Supporting Information:

Supporting Information may be found in the online version of this article.

Correspondence to:

S. Fiedler, stephanie.fiedler@uni-heidelberg.de

Citation:

Fiedler, S., Pham, T. V., Schlund, M., Wahl, S., Sudarchikova, N., Bischof, S., & Hoesly, R. M. (2025). First analysis of climate forcing and response to updated historical anthropogenic aerosol with the new CMIP7 model ICON XPP. *Journal of Advances in Modeling Earth Systems*, 17, e2025MS005067. https://doi.org/10.1029/2025MS005067

Received 5 MAR 2025 Accepted 20 SEP 2025

Author Contributions:

Conceptualization: Stephanie Fiedler Data curation: Rachel M. Hoesly Formal analysis: Trang V. Pham, Manuel Schlund, Sebastian Wahl, Natalia Sudarchikova, Sabine Bischof Funding acquisition: Stephanie Fiedler Methodology: Stephanie Fiedler Resources: Stephanie Fiedler Software: Stephanie Fiedler Supervision: Stephanie Fiedler

© 2025 The Author(s). Journal of Advances in Modeling Earth Systems published by Wiley Periodicals LLC on behalf of American Geophysical Union. This is an open access article under the terms of the Creative Commons Attribution License, which permits use, distribution and reproduction in any medium, provided the original work is properly cited.

First Analysis of Climate Forcing and Response to Updated Historical Anthropogenic Aerosol With the New CMIP7 Model ICON XPP

Stephanie Fiedler^{1,2}, Trang V. Pham³, Manuel Schlund⁴, Sebastian Wahl⁵, Natalia Sudarchikova⁵, Sabine Bischof⁵, and Rachel M. Hoesly⁶

¹Heidelberg University, Institute of Environmental Physics, Heidelberg, Germany, ²GEOMAR Helmholtz Centre for Ocean Research Kiel and Christian-Albrechts-University of Kiel, Faculty of Mathematics and Natural Sciences, Kiel, Germany, ³Deutscher Wetterdienst, Offenbach, Germany, ⁴Deutsches Zentrum für Luft- und Raumfahrt (DLR), Institut für Physik der Atmosphäre, Oberpfaffenhofen, Germany, ⁵GEOMAR Helmholtz Centre for Ocean Research Kiel, Kiel, Germany, ⁶Pacific Northwest National Laboratory, Joint Global Change Research Institute, College Park, MD, USA

Abstract The simple plumes (SP) parameterization for anthropogenic aerosol effects on radiation and clouds has been used in the Coupled Model Intercomparison Project phase six (CMIP6) and beyond. This study documents the new SP forcing data in preparation for use in CMIP phase seven (CMIP7) and its first application in the newly developed coupled atmosphere-ocean-river model ICON XPP. We assess historical trends and spatio-temporal differences for the aerosol optical depth of SP and find moderate differences compared to the CMIP6 data variant of SP. Radiative effects of anthropogenic aerosols from SP are estimated with atmosphereonly experiments of ICON XPP. The global all-sky effective radiative forcing (ERF_{all}) is -0.33 Wm^{-2} for the 2014 anthropogenic aerosols against the pre-industrial level. Using either the CMIP6 version of SP or the different climate state of present-day compared to pre-industrial yield a similar ERF_{all} of anthropogenic aerosol in ICON XPP, with global mean differences of 0.05 Wm⁻². Climate responses to the anthropogenic aerosols are computed with three-member ensembles of fully-coupled historical experiments with ICON XPP. ICON XPP shows no apparent differences in global mean responses for outgoing shortwave radiation, temperature, and precipitation when the updated SP data are prescribed in comparison to experiments that use the CMIP6 variant of SP. Such small present-day differences suggest that future extensions of historical data for SP, not an update of the entire historical period, might be sufficient for climate studies, unless larger revisions of past emissions will be made.

Plain Language Summary The radiative forcing of anthropogenic aerosols is estimated with updated simple plumes data in the new climate model ICON XPP. ICON XPP and updated aerosol data assessed in this study will be used for CMIP7 experiments. This study tests the new aerosol data in the model and documents for instance differences compared to results from the CMIP6 aerosol data. In ICON XPP, the radiative forcing from anthropogenic aerosols due to clouds is lower than in other models that participated in CMIP6. The updated and extended historical data for the simple plumes parameterization enables climate simulations that yield similar results compared to using the aerosol variant from CMIP6.

1. Introduction

Anthropogenic aerosol regionally counteracts warming caused by greenhouse gases. Regional climate responses to aerosol are considered to be large enough that further improvements in air quality could lead to additional warming in the coming decades, which is currently suppressed by aerosol effects (Samset et al., 2024). The exact magnitude of the aerosol radiative forcing (Bellouin et al., 2020) and its associated regional climate responses to aerosols (Wilcox et al., 2023) are still uncertain in our scientific understanding. Uncertainties are for instance evident in the persistent scatter in climate model results for aerosol radiative forcing (C. J. Smith et al., 2020) and known structural deficiencies of CMIP-class models in simulating some of the physical processes involved in aerosol effects, for example, cloud occurrences and their characteristics (Tselioudis et al., 2021; Vignesh et al., 2020).

Simplification of the representation of aerosols in some climate models was instrumental to quantify the model spread arising from other simulated processes. With this purpose in mind, the simple plumes (SP)

FIEDLER ET AL. 1 of 22

Validation: Stephanie Fiedler, Trang V. Pham, Manuel Schlund, Sebastian Wahl, Natalia Sudarchikova, Sabine Bischof Visualization: Trang V. Pham, Manuel Schlund, Sebastian Wahl, Natalia Sudarchikova, Sabine Bischof Writing – original draft: Stephanie Fiedler Writing – review & editing: Stephanie Fiedler, Trang V. Pham, Manuel Schlund, Sebastian Wahl, Natalia Sudarchikova, Sabine Bischof, Rachel M. Hoesly

parameterization (Stevens et al., 2017) was developed and used in a subset of experiments called RFMIP-SpAer in the CMIP6-endorsed Radiative Forcing Model Intercomparison Project (RFMIP, Pincus et al., 2016). The SP parameterization mimics the spatio-temporal changes in anthropogenic aerosols concerning their optical properties and effects on clouds (Stevens et al., 2017). Using SP with a scaling based on CMIP6 emission data (SPv1) in climate models helped to explain differences in the effective radiative forcing of anthropogenic aerosols over the historical time period in RFMIP-SpAer (Fiedler et al., 2023).

SPv1 was also implemented in models for other research interests than for RFMIP-SpAer. Two examples are the representation of anthropogenic aerosols in CMIP6 DECK experiments (Eyring et al., 2016) of the Max-Planck-Institute for Meteorology Earth System Model version 1.2 (MPI-ESM1.2, Mauritsen et al., 2019) and in the atmospheric model ICON-A for climate studies (Giorgetta et al., 2018). For that reason input data for SPv1 for years after 2014 were developed that mimic the future emission changes as projected by CMIP6 scenarios (Fiedler, Stevens, et al., 2019). The use of SPv1 in MPI-ESM1.2 and other CMIP-class models has further led to the request for new input data, for example, in the framework of CovidMIP (Lamboll et al., 2021) to represent the effects of the emission reductions due to lockdowns during the pandemic in EC-Earth3 (Fiedler et al., 2021) and other models (Jones et al., 2021). Moreover, SPv1 has been used as reference data set for a CMIP6 model evaluation (Michou et al., 2020).

Using SPv1 was also tested outside of CMIP for improving satellite-derived data of surface solar radiation within the EUMETSAT Satellite Application Facility on Climate Monitoring (CM SAF). Climatological aerosol information from SPv1 was used for the generation of the surface irradiance data from the CLARA-A3 data record (Karlsson et al., 2023). Moreover, the time series of the monthly aerosol from SPv1 has been used in the generation of the CM SAF Landflux data record (Moutier et al., 2024). Using the temporally changing aerosol information improved the comparison of the decadal trend of surface irradiance with surface reference measurements in Europe and allowed an estimation of the impact of the direct aerosol effect on surface irradiance (Schilliger et al., 2024).

The design of SP based on mathematical functions and the offline driver for the SP code allow users to create their own aerosol plumes and run the parameterization without the need to use SP always together with the comprehensive code of a climate model. It simplifies the design and tests of SP data for diverse applications, for example, for user-generated aerosol information. This characteristic of SP was meant to facilitate experimentation. It has for instance been used for performing experiments for a better understanding of influences of internal variability and aerosol effects on clouds on the magnitude of aerosol forcing (Fiedler et al., 2017), impacts of model dynamics on climate responses associated with aerosol (Nordling et al., 2019), climate responses to different historical patterns of aerosol (Fiedler & Putrasahan, 2021), and climate responses to the location of absorbing aerosols (Williams et al., 2022).

In preparation for CMIP7, modeling centers have requested an update and extension of the historical and scenario data for SP for climate change experiments. There is also the desire for climate forcings for seasonal to decadal climate predictions by the Lighthouse Activity "Explaining and Predicting Earth System Change" of the World Climate Research Programme. In this context, the here-presented new SP variant is currently being tested in the climate prediction systems at the European Center for Medium-Range Weather Forecasting (ECMWF) and the Barcelona Supercomputing Center (BSC).

To serve the community, the objectives of this study are twofold. The main aim is to document and evaluate the first updated and extended historical data for SP (SPv2) for 1850–2020 inclusive (Fiedler & Sudarchikova, 2024), compared to SPv1 that used observationally based emissions until 2014 inclusive (Stevens et al., 2017). SPv2 is consistent with the most recent release of the Community Emissions Data System (CEDS, R. Hoesly et al., 2024), first used as the historical anthropogenic forcing data set in CMIP6 (R. M. Hoesly et al., 2018) and continuously updated and extended in preparation for CMIP7, that is, additional updates in historical emissions will be made. The new CEDS data includes revised emissions, for example, from metal smelting, for the historical period and provides observationally based data for years after 2014, which was the last year in the CMIP6 historical forcings. The updated and extended CEDS emissions give reason to create the new SPv2 data to warrant a high degree of consistency across CMIP6plus and CMIP7 climate forcings data sets. Differences can for instance be expected after 2010, when SO₂ emission estimates decline more quickly in the new CEDS data compared to CMIP6.

FIEDLER ET AL. 2 of 22



We document and evaluate the characteristics of the SPv2 data and the associated climate response against 25 different observation and model data sets. The evaluation of SPv2 includes first estimates of the anthropogenic aerosol radiative effects and historical climate responses with Germany's new seamless prediction model ICON in the eXtended Prediction and Projection configuration ICON XPP (Müller, Lorenz, et al., 2025), which will be used for CMIP7 experiments (Dunne et al., 2024). In the analysis of ICON XPP output, we address the influence of a different climate base state and spatial patterns of anthropogenic aerosols on the radiative forcing and climate responses. The second aim is to address the need for either providing regular updates of the entire historical data or for extensions of previously existing historical anthropogenic aerosol data as provided by SP, which can use new emission data for the historical period when they become available. To that end we evaluate time series of SPv2 against SPv1 data, and compare regional aerosol trends from SPv1 by extending the CMIP6 historical data with CovidMIP future scenarios (Fiedler et al., 2021) and CMIP6 future scenarios (Fiedler, Stevens, et al., 2019) after 2014 against observation data and SPv2. Moreover, we assess the SP version-induced differences in the simulated climate side by side to the present-day model biases of ICON XPP.

2. Methods and Data

2.1. CEDS Emission Data

We use updated and extended CEDS emission data for anthropogenic short-lived climate forcers (source ID CEDS-CMIP-2024-11-25, R. Hoesly et al., 2024) for the historical time period. Anthropogenic forcing data has been updated multiple times since the release of CMIP6 forcing data, extending data to new years as well as revising underlying historical energy data, fuel properties, and emission factors as better data becomes available. Since CMIP6, updated forcing data for the historical emissions before 2000 for SO₂, NH₃, CH₄, and CO₂ have been similar. Globally, revised CO emissions trends in the last 50 years are smaller, particularly from transportation in Latin America, Former Soviet Union, and Asia (not including China). Since 2000, revised emissions trends from residential sector in China have contributed to a steep global decline in CO in updated forcing data. NO_x emissions have also seen a steep decline in China since 2000, mostly from industry and energy transformation sectors, NMVOCs have reduced by almost 20% in the later half of the 1900s in the forcing data, largely due to revised historical trends for transportation and energy transformation across Asia. Revisions in BC and OC emissions in China in the residential, commercial and energy transformation sectors have led to significantly lower emissions trends especially after 2000. Previous trends indicated swiftly increasing BC and OC emissions but more updated trends show steady declines in recent years. Significant revisions across regions in residential biomass estimates have led to global decreases in BC and OC, especially in the last 50 years. Updated NH₃ emissions are similar to CMIP6 estimates, with new trends only a few percent lower than previous trends in recent years, largely due to updated waste estimates, although these are still prone to uncertainty.

Of particular interest for SPv2 are differences in the SO₂ emissions forcing data since CMIP6, since it is the primary control for differences in the temporal scaling of the aerosol optical depth. The spatial allocation of CEDS emissions for SO₂ has been improved compared to CMIP6 historical data, with the introduction of the SO₂ catalog from the Ozone Monitoring Instrument (OMI, Fioletov et al., 2023) for sources in the gridding method. Globally, SO₂ emissions used here are very similar to previous forcings data until the late 2000s, but not for the same reasons. Historical estimates of industrial SO₂ emissions increased by a similar amount as energy transformation estimates decreased from 1850 through 1950 due to revisions in historical smelting and sulfur contents. In the late 2000s, global SO₂ emissions decrease more quickly than in the CMIP6 forcings data, due to revised trends in China for both industry and energy transformation sectors. Both sectors maintain similar trajectories through 2020, where emissions trends flatten post the Covid pandemic. International shipping data are slightly larger compared to CMIP6 forcings data from 1990 onward and show a significant reduction in 2020.

2.2. Simple Plumes Parameterization

We use the simple plumes (SP) parameterization code, which was developed at the Max-Planck-Institute for Meteorology. The code of SP (Stevens et al., 2017) has not been modified in the present study (Section 2.2.1), but new input data for the historical time period is generated (Section 2.2.2). In summary, there are two differences compared to the historical data from Stevens et al. (2017). First, the historical data are longer in SPv2 (1850–2020) compared to SPv1 (1850–2014), and consistent with CMIP6plus emissions data (Section 2.1) instead of

FIEDLER ET AL. 3 of 22

CMIP6. Second, we use the scaling method for gridded emission data in SPv2 consistent with the method for future scenarios (Fiedler, Stevens, et al., 2019), rather than country-aggregated values as in SPv1.

2.2.1. Characteristics

Characteristics of SP are technically documented at length by Stevens et al. (2017) and are summarized in the following. SP uses mathematical functions to create the plume shapes of the aerosol extinction, namely Gaussian functions in the horizontal distribution and beta functions for the vertical profiles. The use of mathematical functions allows the parameterization to be independent of model specific configurations in the sense that the created aerosol fields automatically adjust to the host model's spatial and temporal resolutions and the wavelengths bands in the radiative transfer calculations. It makes the parameterization flexible and representing aerosols in climate models relatively easy, for example, a preprocessing of the aerosol data for model-specific resolutions and wavelengths is obsolete when SP has been implemented.

SP provides wave-length dependent anthropogenic aerosol extinction profiles as monthly means to create the characteristic seasonal cycles for the plumes, for example, reproducing seasonally active biomass burning in Africa and South America (Stevens et al., 2017). The monthly climatology of the anthropogenic aerosol optical depth (τ_a) at 550 nm for 2005 in SPv1 was adjusted to the Max-Planck-Institute for Meteorology Aerosol Climatology (MAC, Kinne et al., 2013; Kinne, 2019). Values for τ_a at other wavelengths are computed assuming a constant Ångstrom exponent of $\alpha = 2.0$. The single scattering albedo is 0.93 for plumes dominated by industrial pollution and 0.87 for plumes with aerosol contributions from biomass burning in the tropical belt. The asymmetry parameter is a globally constant value of 0.63.

In addition to the anthropogenic aerosol optical properties, SP provides spatio-temporal dependent factors η_N to induce anthropogenic aerosol effects on clouds by multiplying η_N with the cloud droplet number concentration (N) in the host model. The factor η_N can be used in the radiative transfer parameterization as an effective parameter for aerosol effects on the cloud albedo (Twomey, 1974), for example, as in MPI-ESM1.2 (Fiedler et al., 2017), or in the cloud microphysical parameterization to induce additional cloud adjustments, for example, as in EC-Earth3 (Fiedler et al., 2021). It is possible to change the simulated magnitude of aerosol effects on clouds from SP (Fiedler et al., 2017), which remains a large uncertainty in the understanding of aerosol forcing (Bellouin et al., 2020). Year-to-year changes are described by a time-dependent scaling factor for each plume that adjusts τ_a in the plume centers over the years. The scaling factors are derived from monthly data from CEDS emissions for SO₂ and NH₃, for example, prepared for CMIP6 (R. M. Hoesly et al., 2018).

2.2.2. Update and Extension

We retain all characteristics of SPv1 for SPv2 except for the temporal scaling over the historical period. In the CMIP6 version SPv1, earlier referred to as MACv2-SP, the temporal scaling was based on the CMIP6 historical data for 1850–2014 inclusive (Stevens et al., 2017) and the future scenarios of CMIP6 for 2015–2100 inclusive (Fiedler, Stevens, et al., 2019). Specifically, the historical evolution of τ_a of SPv1 is scaled with country-aggregated CEDS emissions for SO₂ and NH₃ (Stevens et al., 2017). For the SPv2 data, we update and extend the historical scaling factors for the decadal changes in τ_a from 1850 to 2020, using gridded data for emissions of SO₂ and NH₃ taken from the CEDS emissions for anthropogenic short-lived climate forcers (source ID CEDS-CMIP-2024-11-25, R. Hoesly et al., 2024). We annually integrate the monthly emission fluxes across all sources for SO₂ and for NH₃. The grid of the CEDS emission data has a horizontal resolution of 0.5°. By applying conservative remapping, we spatially interpolate the annual values to a coarser horizontal grid with 96 latitudes and 192 longitudes, for consistency with the method applied to gridded emissions for future scenarios of SPv1 (Fiedler et al., 2021; Fiedler, Stevens, et al., 2019).

The scaling factors are then computed following the method for the historical data of SPv1 (Stevens et al., 2017) but adjusted to using gridded emissions as in the future scenarios for SPv1 (Fiedler, Stevens, et al., 2019). The processing steps are as follows. First, we compute emission anomalies relative to 1850 by subtracting the emission of 1850 from the time series of annual emission sums for SO_2 and NH_3 . This step is motivated by the intended use of SPv2 for historical experiments that are initialized with data from the model's own pre-industrial control experiments, which include tropospheric aerosols for the pre-industrial state. The pre-industrial aerosol mixture is dominated by natural aerosols and may regionally include anthropogenic aerosols from emissions in 1850. Second, we spatially average the emissions over 10×10 grid boxes around each plume center and compute

FIEDLER ET AL. 4 of 22

Table 1Overview of ICON-NWP Atmosphere-Only Experiments for Radiative Forcing Calculations

| Experiment | Years | Sea surface temperature and sea ice climatology | Anthropogenic aerosol | Other forcings |
|-------------------|-------|---|-----------------------|----------------|
| piClim-Control | 120 | 1870-1880 (D. M. Smith et al., 2019) | - | 1850 |
| piClim-CMIP6-2014 | 30 | 1870-1880 (D. M. Smith et al., 2019) | 2014, SPv1 | 1850 |
| piClim-CMIP7-2014 | 30 | 1870-1880 (D. M. Smith et al., 2019) | 2014, SPv2 | 1850 |
| piClim-CMIP6-1975 | 30 | 1870-1880 (D. M. Smith et al., 2019) | 1975, SPv1 | 1850 |
| piClim-CMIP7-1975 | 30 | 1870–1880 (D. M. Smith et al., 2019) | 1975, SPv2 | 1850 |
| piClim-CMIP7-2020 | 30 | 1870–1880 (D. M. Smith et al., 2019) | 2020, SPv2 | 1850 |
| pdClim-Control | 120 | 1980–2012 (K. Taylor et al., 2015) | - | 2014 |
| pdClim-CMIP6-2014 | 30 | 1980–2012 (K. Taylor et al., 2015) | 2014, SPv1 | 2014 |

Note. A monthly sea-surface temperature (SST) and sea-ice climatology are prescribed as averages computed over the listed time periods. Anthropogenic aerosols from SPv1 (Stevens et al., 2017) or SPv2 (Fiedler & Sudarchikova, 2024) are prescribed as an annually repeating monthly climatology for the listed year. All other climate forcings are fixed at pre-industrial (1850) or present-day (2014) level.

10-year running means for smoothing spatio-temporal variability in the emissions. Third, we compute the scaling factors as fractional differences in the emission anomalies relative to the emissions of 2005. The year 2005 is the reference year of the monthly climatology of τ_a that was also used in SPv1. The emissions for SO₂ have a higher relative weight of 0.645 than NH₃ in computing the scaling factors as in SPv1 (Stevens et al., 2017). The generated scaling factors have here a decadal resolution and the MACv2-SP code linearly interpolates the values in between. SP data sets with higher temporal resolution are available, for example, for CovidMIP (Fiedler et al., 2021), and for the years after 2020 for the SPv2.1 historical forcing data set for use in CMIP7 (Fiedler & Azoulay, 2025).

2.3. Evaluation Strategy

We test the new SPv2 data in a contemporary climate model in preparation of CMIP7. To that end, we use the newly developed Earth system model "ICOsahedral Non-hydrostatic eXtended Prediction and Projection" (ICON XPP, Müller, Lorenz, et al., 2025) in fully coupled and atmosphere-only configurations. The atmosphere-only experiments, listed in Table 1, are used to calculate the sensitivity of the effective radiative forcing (ERF) of anthropogenic aerosols to different base states, different aerosol patterns, and the two data versions of SP (Section 2.3.1). The results for the radiative forcing are evaluated against similar experiments with SP in CMIP6 models published in earlier studies. Moreover, ensembles of historical experiments with the fully coupled Earth system model ICON XPP (Table 2) allow us to assess the sensitivity of the climate response to the SP versions (Section 2.3.2).

In total, we use 25 different reference data sets from satellite products, reanalysis data and climate model output including multi-model ensembles from CMIP and AeroCom to evaluate the results with SPv2. We intercompare the present-day total aerosol optical depth (τ) and past climate change signatures for outgoing shortwave radiation, temperature, precipitation, and cloud cover. Data intercomparisons for ICON XPP are facilitated by applying the Earth System Model Evaluation Tool (ESMValTool, Righi et al., 2020; Andela et al., 2024b), which is a community diagnostic and performance metrics tool for the evaluation and analysis of Earth system models. ESMValTool has recently been extended to be able to process ICON XPP output without any postprocessing (Schlund et al., 2023). Specifically, the results from the ICON XPP historical experiments are evaluated against output from the historical experiments of CMIP6 (Eyring et al., 2016) and reference data listed in Table 3.

 Table 2

 Historical Climate Change Experiments With ICON XPP

| Experiment | Period | Ensemble size | Anthropogenic aerosol | Other forcings |
|------------|-----------|---------------|-------------------------------------|----------------|
| hist-SPv1 | 1850-2020 | 3 | SPv1 (Stevens et al., 2017) | as in CMIP6 |
| hist-SPv2 | 1850-2020 | 3 | SPv2 (Fiedler & Sudarchikova, 2024) | as in CMIP6 |

FIEDLER ET AL. 5 of 22

 Table 3

 Overview of Climate Data as Observational References

| Data set | Variable(s) | Type | Years | Reference |
|-------------------|---|-----------------|-----------|-------------------------|
| CERES-EBAF Ed4.2 | Outgoing shortwave radiation at the top of the atmosphere | Satellite | 2001–2022 | Loeb et al. (2018) |
| ERA5 | Near-surface air temperature precipitation | Reanalysis | 1979–2021 | Hersbach et al. (2020) |
| GPCP-SG v2.3 | Precipitation | Satellite-gauge | 1979–2022 | Adler et al. (2017) |
| HadCRUT5 v5.0.1.0 | Near-surface air temperature | Ground | 1979–2021 | Morice et al. (2021) |
| ISCCP-FH | Outgoing shortwave radiation at the top of the atmosphere | Satellite | 1984–2016 | Zhang and Rossow (2023) |
| ESA CCI | Total cloud cover | Satellite | 2002–2016 | Stengel et al. (2020) |
| MODIS | Total cloud cover | Satellite | 2003–2018 | Platnick et al. (2003) |

The new SPv2 data are evaluated based on the total aerosol optical depth (τ) , which includes both natural (τ_n) and anthropogenic (τ_a) aerosols. To obtain total τ for both SP versions, we add the monthly climatology for τ_n from Kinne (2019) to the corresponding monthly data for τ_a from SPv2 and SPv1. The results for global mean τ are compared against reference data sets from Table 4, previously collected and assessed in Vogel et al. (2022). We use the same data and method for averaging τ as in Vogel et al. (2022). Multi-model means of CMIP5 and CMIP6 equally weight individual models by using one historical simulation per model (Tables S1-S2 in Vogel et al., 2022).

2.3.1. Radiative Forcing

We perform atmosphere-only experiments with ICON XPP to estimate radiative forcing from SP. The atmospheric model of ICON XPP is called ICON-NWP (Zängl et al., 2015). In the ICON-NWP model configuration

Table 4Data for Total Aerosol Optical Depth (τ) , Including Anthropogenic (τ_a) and Natural Aerosol in the Troposphere (τ_n) , Following Vogel et al. (2022)

| Data set | Туре | Period | Reference |
|-------------|-------------------------------|-----------|---------------------------------|
| AeroCom-I | Aerosol-climate models output | 2000 | Schulz et al. (2006) |
| AeroCom-III | Aerosol-climate models output | 2010 | Gliß et al. (2021) |
| CMIP5 | Aerosol-climate models output | 1995–2005 | K. E. Taylor et al. (2012) |
| CMIP6 | Aerosol-climate models output | 1995–2014 | Eyring et al. (2016) |
| ICAP | Operational ensemble output | 2015 | Xian et al. (2019) |
| CAMS | Reanalysis product | 2003-2022 | Inness et al. (2019) |
| MERRA-2 | Reanalysis product | 1995–2023 | Gelaro et al. (2017) |
| MAC-v2 | Climatology | 2005 | Kinne (2019) |
| SPv1 | SPv1 for τ_a | 1850-2014 | Stevens et al. (2017) |
| | Climatology for τ_n | | Kinne (2019) |
| SPv2 | SPv2 for $	au_a$ | 1850-2020 | Fiedler and Sudarchikova (2024) |
| | Climatology for τ_n | | Kinne (2019) |
| FMImerge | Merged satellite products | 1998–2017 | Sogacheva et al. (2020) |
| AATSR | Satellite product | 2002-2012 | North et al. (1999) |
| CALIPSO | Satellite product | 2007–2019 | Winker et al. (2010) |
| MISR | Satellite product | 2001–2019 | Kahn et al. (2005) |
| MODIS Aqua | Satellite product | 2003-2019 | Levy et al. (2007) |
| MODIS Terra | Satellite product | 2003-2019 | Levy et al. (2007) |
| POLDER | Satellite product | 2006-2011 | Chen et al. (2020) |
| SeaWiFS | Satellite product | 1998–2010 | Hsu et al. (2012) |
| SLSTR | Satellite product | 2018–2019 | North et al. (2021) |

FIEDLER ET AL. 6 of 22

used here, radiation calculations are performed with ecRad (Hogan & Bozzo, 2018; Rieger et al., 2019) and cloud microphysics following Seifert and Beheng (2006). Natural aerosols are prescribed as monthly climatology of aerosol optical properties for the wave lengths of ecRad based on data from MAC (Kinne, 2019). Anthropogenic aerosols are represented with the SP parameterization (Section 2.2). Radiative forcing calculations are performed with contemporary methods, namely instantaneous radiative forcing (IRF) and the fixed sea-surface temperature method for ERF (Fig. 3 in Fiedler et al., 2024).

We calculate the ERF of anthropogenic aerosols using the experiments with prescribed sea-surface temperatures and sea-ice, for example, for the pre-industrial (piClim) or present-day (pdClim) climate state. The setup of piClim experiments for forcing calculations was established in CMIP6 (Forster et al., 2016) and is part of the experiment request of CMIP7 (Dunne et al., 2024). The sea surface temperatures and sea ice are prescribed as a monthly mean climatology which is annually repeated in the simulations. That climatology is computed here over 1870–1880 for data from the Polar Amplification MIP (UCI-PAMIP v1.0, D. M. Smith et al., 2019) for the piClim experiments, and over 1990-2012 for data from the atmosphere MIP (PCMDI-AMIP v1.1.7, K. Taylor et al., 2000, 2015) for what we call pdClim experiments. Prescribing the climatology eliminates the influence of potential model biases in the simulated sea-surface state on the ERF estimates. It is a different approach to RFMIP (Pincus et al., 2016), where the model's own sea-surface temperature and sea ice were prescribed as monthly climatology computed from output of fully coupled atmosphere-ocean experiments. Comparing the results from pdClim and piClim experiments allows us to analyze the dependency of the aerosol radiative forcing on the climate base state in ICON-NWP. All our piClim and pdClim experiments are performed on 90 vertical levels in the atmosphere and the triangular horizontal grid R2B4 of ICON-NWP, which corresponds to an approximate resolution of 160 km. Climate forcings except for anthropogenic aerosols are from CMIP6 for 1850 in piClim and for 2014 in pdClim. Anthropogenic aerosol data are from SPv1 or SPv2 for the years 1975, 2014, or 2020 as listed in Table 1 and prescribed as annually repeating monthly climatology, for example, monthly aerosol data of the year 2014 from SPv2 in piClim-CMIP7-2014.

Effective radiative forcing for all sky (ERF_{all}) and clear sky (ERF_{clear}) are computed as the difference in the shortwave radiation budget at the top of the atmosphere between the experiment with anthropogenic aerosols against the corresponding control experiment with 1850 aerosol level, for example, pdClim-CMIP6-2014 against pdClim-Control and piClim-CMIP7-2020 against piClim-Control. For all-sky conditions, the calculation of the radiative transfer is performed for both the cloudy and cloud-free atmospheric column. The simulated clouds are assumed to be transparent for radiation in a diagnostic call of the radiative transfer calculation to compute the clear-sky radiative effects of anthropogenic aerosols. We follow the approach to sample model internal variability in the radiation budget like in Fiedler et al. (2017). The experiments piClim-Control and pdClim-Control are relatively long with 120 years each, which is an effective way to create reference data for computing ERF. Each of the experiments with added anthropogenic aerosols is shorter with a length of 30 years. These experiment lengths create enough model output to compute the radiative forcing with substantially reduced influence of natural internal variability in the radiation budgets on aerosol ERF (Fiedler et al., 2017). The first year of each simulation is considered as spin-up period and excluded prior to the data analyses. A 1-year spin-up is generous because the atmosphere more quickly compensates initial disturbances. Aerosol effective radiative effects are computed as annual differences in the radiation budget and averaged over all years thereafter to obtain mean spatial patterns. Spatial averages of the latter determine the global mean ERF. Note that the experiments for this study were created for testing SPv2 prior to the use in CMIP7, when the ICON-NWP model version and CMIP7 boundary data were not final. Aerosol forcing estimates from ICON XPP (Section 2.3.2) in CMIP7 might therefore not be identical with the here reported values.

We further compute the instantaneous radiative forcing in all-sky conditions (IRF $_{all}$) and the net contribution from rapid adjustments (ADJ $_{all}$). Values for IRF $_{all}$ of anthropogenic aerosols are calculated in all experiments with anthropogenic aerosols through double calls to the radiative transfer calculation. One of these calls are free of anthropogenic aerosol whereas the other call includes the aerosol for the same atmospheric state. The difference in the radiation budget between the two calls determines IRF $_{all}$. The values for ADJ $_{all}$ are computed as the difference of ERF $_{all}$ against IRF $_{all}$.

FIEDLER ET AL. 7 of 22

2.3.2. Climate Response

The SP data were utilized in experiments with the new fully coupled atmosphere-ocean-river model system ICON XPP (Müller, Lorenz, et al., 2025). ICON XPP uses the atmosphere component ICON-NWP (Section 2.3.1). Land surface processes are simulated with the "Jena Scheme for Biosphere Atmosphere Coupling in Hamburg" (JSBACH, Schneck et al., 2022). The ocean-sea ice component of ICON XPP is from the ocean general circulation model of the Max-Planck Institute for Meteorology (ICON-O, Korn et al., 2022), and the "Hydrological Discharge model" from the Helmholtz-Zentrum Hereon (HD, Hagemann et al., 2023).

ICON XPP has been integrated over time with annually repeating pre-industrial conditions as of 1850 by the model partners (Müller, Lorenz, et al., 2025). At the end of that pre-industrial control experiment, ICON XPP has achieved a stable climatology without drift, meeting all key benchmarks, including near-surface air temperature, net radiation at the top of the atmosphere, Atlantic Meridional Overturning Circulation (AMOC), and sea-ice properties. The model configuration used has a horizontal resolution of 80 km (R2B5) in the atmosphere, 20 km in the ocean (R2B7), and 50 km in the river routing model. The atmosphere comprises 130 vertical levels extending up to 75 km. Detailed information on the tuning of ICON XPP and the control experiments is available from Müller, Lorenz, et al. (2025).

Building on the pre-industrial control experiment, two sets of historical experiments with transient changes in climate forcings were performed for the present study, each with three ensemble members. The two ensembles of historical experiments differ only in the anthropogenic aerosol data with one using SPv1 (hist-CMIP6) and the other SPv2 (hist-CMIP7). All ICON XPP historical simulations cover the period 1850–2020 inclusive. The transient climate forcings for irradiance, land cover, ozone, volcanic aerosol, and greenhouse gas concentrations are as for CMIP6 simulations. Since the CMIP6 forcing data end in 2014, forcing data of 2014 were also used as boundary condition for the last years of the hist-CMIP6 and hist-CMIP7 simulations (2015–2020). For 2015–2020, SPv1 prescribes transient changes for the anthropogenic aerosols following SSP2-4.5 (Fiedler, Stevens, et al., 2019).

3. Results

3.1. Aerosol Properties

3.1.1. Mean Differences

Updating the input data for the simple plumes parameterization (SPv2) using the CEDS emission data for historical experiments has moderate influence on τ_a and η_N , compared to the MACv2-SP data for CMIP6 historical experiments (here SPv1, Stevens et al., 2017). The global spatial patterns of the resulting τ_a and η_N (Figure 1) reflect the spatio-temporal development of emissions of SO₂ and NH₃ in the historical period. Compared to NH₃, the larger SO₂ emission fluxes and larger weight in the relative contribution to the τ_a plumes primarily determine the τ_a patterns of SP. The latter have strongly changed in the past with most emission in Europe and North America during the 1970s, whereas most emissions in the first two decades of the 21st century occur in Eastern Asia. The shift in emissions for anthropogenic aerosol leads to the temporal changes in the spatial pattern of τ_a and η_N (Figure 1) that are broadly consistent with SPv1 (Figure S1 in Supporting Information S1).

Although the spatial patterns in SPv2 are similar compared to SPv1, magnitudes of τ_a are regionally different by up to $\Delta\tau_a=\pm0.05$ (Figure 2). Regionally larger τ_a in SPv2 are seen for years between 1900 and 1990 in Europe, Southern central Africa, and North Africa (Figures 2a and 2b). This finding is consistent with additionally available emission data from metal smelting in the updated CEDS data set (R. Hoesly et al., 2024). More emission data since CMIP6 has become available for point sources for metal smelting in Serbia and Africa and have been associated with copper production. In SPv2, the largest differences in regional τ_a of up to $\Delta\tau_a=0.05$ are seen around the 1970s (Figure 2b), at the time when anthropogenic aerosol pollution was relatively high over Europe with $\tau_a\approx0.3$. Moreover, the anthropogenic aerosol effects on clouds are relatively high in the European plume during the period 1960–2000 with a maximum of $\eta_N\approx1.4$. The maxima in the European plume have been superseded by the East Asian plume in 1990 with a maximum of $\eta_N>1.4$ around 2010, and a sharp decrease thereafter until 2020 (Figure 2c). Regionally smaller τ_a is seen in the East Asian plume in SPv2 compared to SPv1 after 2010. Toward the end of the time series in 2020, the South Asian plume has $\tau_a\approx0.2$ and $\eta_N\approx1.35$ which is comparable to East Asia. East and South Asia share together the largest values for τ_a and η_N in 2020. The next largest $\tau_a<0.15$ in 2020 is seen in the Africa plumes with positive trends since the 2000s.

FIEDLER ET AL. 8 of 22

0.0

 T_a

 $\eta_{_{N}}$

1975

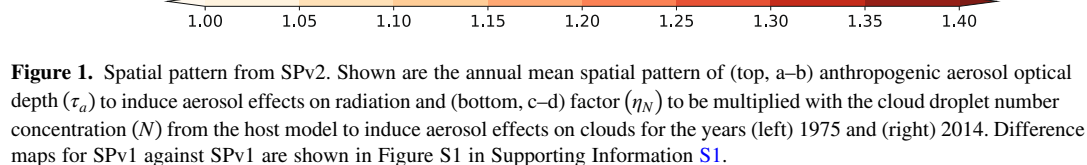
0.1

0.2

2014

0.5

19422466, 2025, 10, Downloaded from https://agupubs.onlinelibrary.wiley.com/doi/10.1029/2025MS005067 by Drech Zentrum F. Luft-U. Raum Fahrt In D. Helmholtz Geneim, Wiley Online Library on [24/10/2025]



1.076

b)

0.4

d)

0.0254

0.3

We evaluate the representation of τ_a using observational data products from satellites and reanalysis (Figure 3). It requires adding a background climatology for natural aerosols in the troposphere for τ_n to obtain a total aerosol optical depth τ . For estimating τ , we add the monthly data from MAC to SPv1 and SPv2. MAC is chosen since it was used together with SPv1 in global climate model experiments in past studies (e.g., Fiedler et al., 2021;

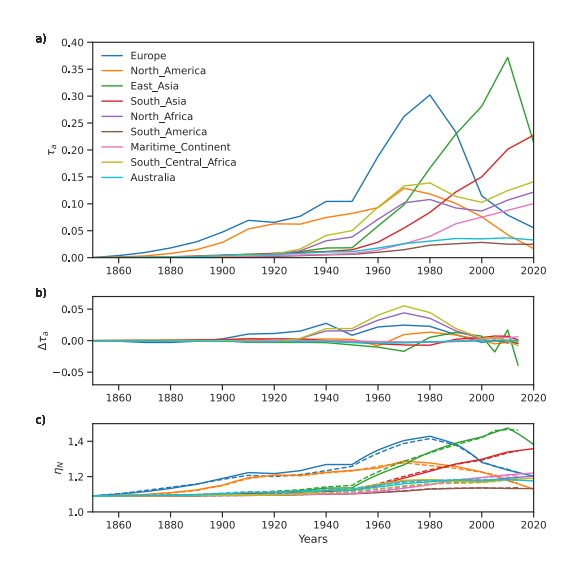


Figure 2. Regional τ_a and η_N . Shown are τ_a of anthropogenic aerosols averaged around the color-coded aerosol plume centers within a distance of 10° (a) for SPv2 and (b) for SPv2 minus SPv1, and (c) η_N for SPv2 (solid lines) and SPv1 (dashed lines).

Giorgetta et al., 2018; Mauritsen et al., 2019) and in the present study together with SPv2 in ICON XPP experiments. We compare against nine τ data sets, following those used in Vogel et al. (2022) and listed in Table 4. Differences in τ across these data sets serve as an estimate of observational uncertainty.

Annual mean $\tau \approx 0.14$ from both SPv1 and SPv2 plus MAC fall within the observational differences of $\tau \approx [0.12, 0.17]$ between 1998 and 2020, spatially averaged between 60°N and 60°S (Figure 3). The observational differences in global mean τ by about 0.05 across the data sets is up to four times larger than the year-to-year variability captured by individual data sets, for example, a difference in τ by 0.01 in FMImerge between 2012 and 2013 (Figure 3). The τ data from SPv1 and SPv2 plus MAC agree well with the multi-model mean over historical experiments from CMIP5 for 1998-2005 and are smaller by about 0.02 compared to CMIP6 for 1998-2014. Note that the fraction and the degree to which the aerosols absorb radiation vary across CMIP6 models with some CMIP6 models having a positive direct radiative forcing of anthropogenic aerosols (Fiedler et al., 2023), which disagrees with other evidence (Bellouin et al., 2020). Nevertheless the mean τ across CMIP6 historical experiments falls within the observational uncertainty. Observational data for the anthropogenic and natural absorption aerosol optical depth would be useful to better evaluate and constrain the models.

FIEDLER ET AL. 9 of 22

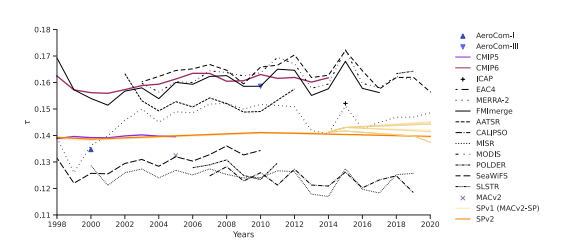


Figure 3. Spatial mean τ . Shown are total τ (anthropogenic plus natural) averaged for the region 60°S to 60°N from different observational and model data sets following Vogel et al. (2022), summarized in Table 4. SPv1 uses the historical data from Stevens et al. (2017) until 2014 and the CMIP6 scenarios from Fiedler, Stevens, et al. (2019) thereafter. SPv1 and SPv2 include here the natural τ climatology from MAC (Kinne, 2019).

3.1.2. Seasonal Differences

The seasonal cycle in SPv2 depends on the plume, with $\tau_a > 0.05$ in the zonal mean around 30°N between March and October and a sharp decrease in τ_a to zonal mean $\tau_a < 0.01$ North of 60°N and South of 0°, averaged for 2000–2014 (Figure 4a). Around the equator, a seasonal maximum in zonal averages of up to $\tau_a \approx 0.07$ occurs from July to September reflecting the seasonally active biomass burning in the tropics, namely in Africa, South America, and Southeast Asia. Compared to SPv1, the overall monthly patterns are similar in SPv2, but there is a moderate shift of τ_a from the northern hemisphere extratropics to the tropics by 1–2% of τ_a in SPv2 (Figure 4b). That increase in the tropics is largest around November with 3% for zonal mean $\tau_a < 0.04$. Earlier in September, the tropical mean South of the equator sees also a slight reduction in τ_a by about -1%. The calculated monthly τ with SPv1 and SPv2

plus MAC fall within the observational uncertainty. Monthly global mean τ differ by about 0.05 across nine different observational data sets (Figure S2 in Supporting Information S1). That value is comparable to maxima in zonal mean τ_a from SPv2 (compare Figure 4a). Although the month-to-month changes in global monthly mean τ are different across the observational data sets, both SP versions plus the natural aerosol from MAC agree on the maximum in August, a secondary maximum in March, and a minimum in November as seen in some of the observational products for τ (Figure S2 in Supporting Information S1).

3.1.3. Trend Differences

The changes in τ from 1998 to 2020 are small and somewhat different in the data sets, averaged between 60°N and 60°S (Figure 3). CMIP6 has a slightly positive trend in mean τ over the period 1998–2014, consistent with a slightly less negative radiative forcing of anthropogenic aerosols over that time period (Fiedler et al., 2023). The magnitude at the upper end of the range in τ and the 1998–2014 trend of τ averaged across the CMIP6 historical experiments agrees well with the observational estimates from FMImerge, MODIS, and AATSR. Other data sets like MERRA2 and MISR have no apparent positive trend in spatially averaged τ for 1998–2014. The projected changes in spatially averaged τ from 2014 to 2020 from SPv1 plus MAC are smaller with differences of about 0.005. Compared to SPv2 plus MAC, τ trends with most SPv1 scenarios are larger and all fall within the observational uncertainty (Figure 3).

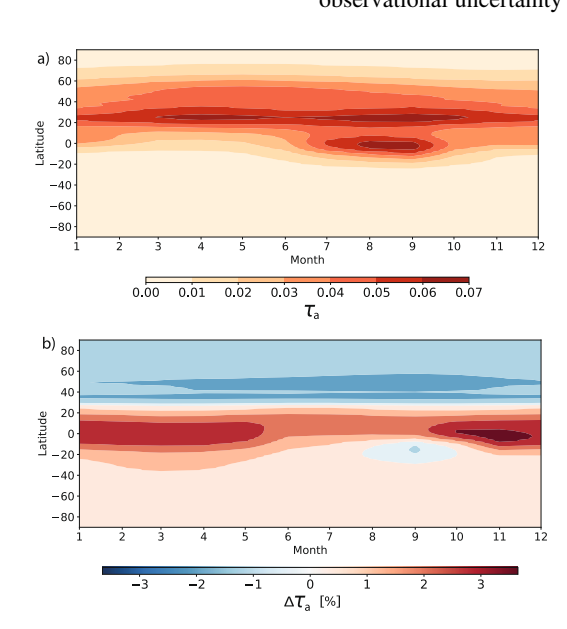


Figure 4. Zonally averaged τ_a of anthropogenic aerosols. Shown are the zonal means of (top) τ_a from SPv2 and (bottom) percentage difference in $\Delta \tau_a$ for SPv2 against SPv1 divided by SPv1, averaged per month over 2000–2014

Regional trends in τ are noticeable in observational data sets, for example, documented for some data sets elsewhere (Cherian & Quaas, 2020; Gupta et al., 2022; Pozzer et al., 2015). We assess to what extent τ_a from SPv2 and SPv1 with post-2014 extensions with future scenarios represent the observed development of τ . The post-2014 extensions for SPv1 use emission data of scenarios created for ScenarioMIP (Gidden et al., 2019) and CovidMIP (Lamboll et al., 2021). Our analysis of the reanalysis data from MERRA2 and CAMS, and satellite data from MODIS and MISR shows an agreement for negative 2003-2019 trends in τ over East Asia, South America, North America and Europe and positive trends around India with values of about $\pm 0.1 \, \tau \, \text{decade}^{-1}$ (Figure S3 in Supporting Information S1). The representation of the 2003–2019 trends in τ_a from SPv1 with the extensions from the scenarios depends on the region (details in Supporting Information S1). The SPv1 extension of τ with the ScenarioMIP scenario SSP2-4.5 yields the highest pattern correlation (0.62) against the observed pattern of trends for 2003-2019, which is similar to SPv2 using observed emissions throughout.

The SPv1 trend of τ for 2010–2022, which includes the reduction in emissions due to lockdowns during the pandemic, is only slightly better with a post-2014 extension from CovidMIP compared to the extension with the best CMIP6 scenario (Figure 5). Specifically, the CovidMIP scenario extension leads to a pattern correlation coefficient for the 2010–2022 trends in τ of 0.7 (Figure 5m), compared against the mean over two reanalysis data sets

FIEDLER ET AL. 10 of 22

1942/466, 2025, 10, Downloaded from https://agupubs.onlinelibrary.wiely.com/doi/10.1029/2025MS005067 by Drsch Zentrum F. Luft-U. Raum Fahrt In D. Helmholtz Gemein., Wiley Online Library on [24/10/2025]. See the Terms and Condition

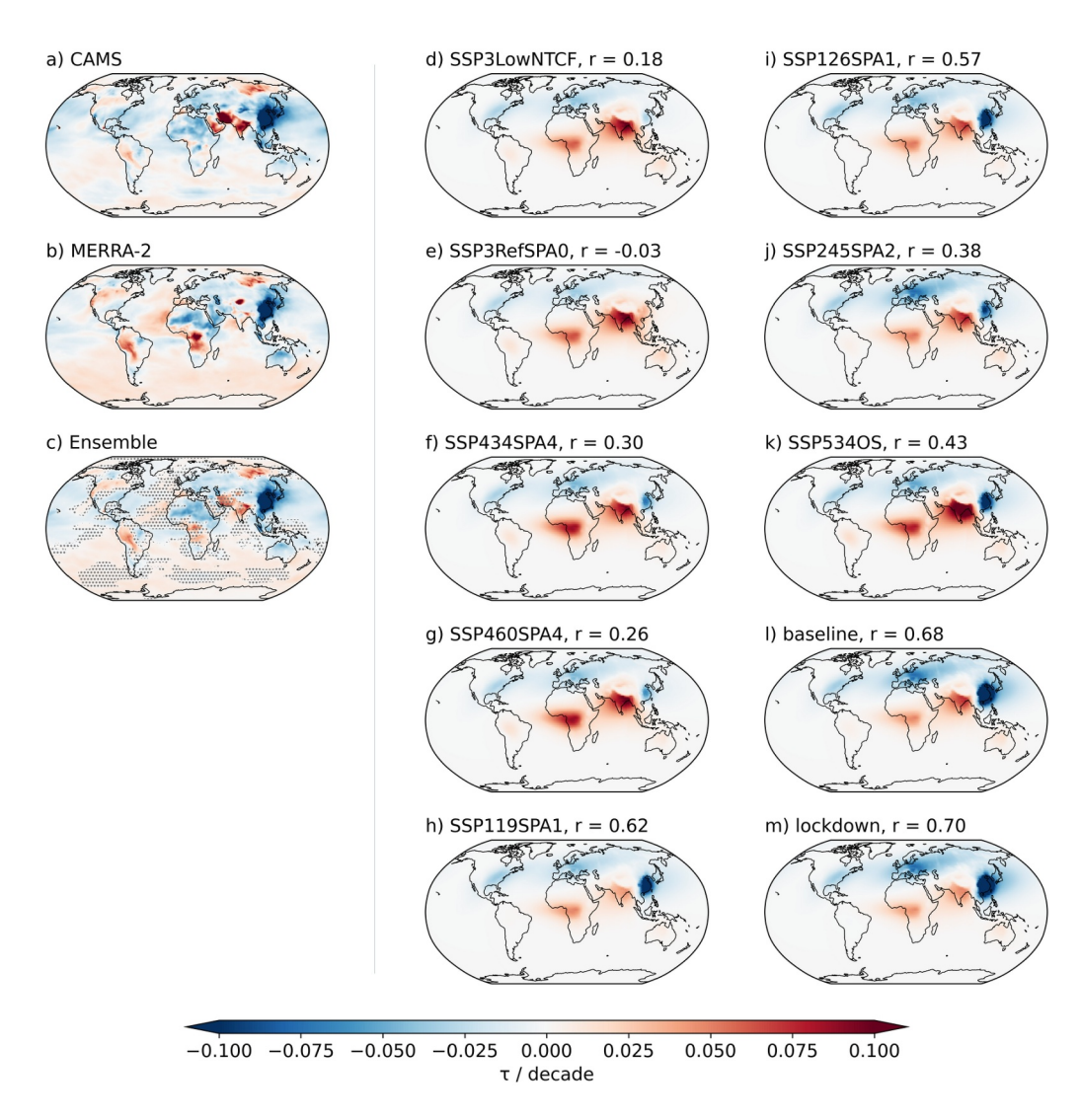


Figure 5. Trends in total τ per decade including the pandemic influence on emissions. Shown are trends in annually averaged total τ (anthropogenic plus natural) for 2010–2022 from (a) CAMS (Inness et al., 2019), (b) MERRA-2 (Gelaro et al., 2017), (c) the mean across the trends in CAMS and MERRA-2, (d–k) SPv1 following the CMIP6 future scenarios (Fiedler, Stevens, et al., 2019) and (l) the CovidMIP baseline/SSP2-4.5 scenario and (m) the CovidMIP scenarios that include a lockdown (Fiedler et al., 2021). For the period considered here the different CovidMIP scenarios including a lockdown have the exact same trends (not shown). Hatching in (c) marks where the reanalysis data sets do not agree on the sign of the trend.

(Figures 5a–5c). By design none of the scenarios for anthropogenic aerosols represent trends in natural τ_n , for example, the decrease in desert-dust aerosols over North Africa from the reanalysis for 2010–2022. Also none of the ScenarioMIP projections of emissions expected the occurrence of a pandemic that would reduce anthropogenic emissions of aerosol. Low pattern correlations like seen for six ScenarioMIP scenarios is therefore to be expected against the observed pattern of τ trends (Figures 5c–5m). Nevertheless the pattern correlation of the trend in τ is 0.57–0.68 in the two SSP1 scenarios (Figures 5h and 5i) and in the baseline of CovidMIP that corresponds to SSP2-4.5 (Figure 51). These values are similar to the projected CovidMIP trends for the lockdown (Figure 5m), although the underlying assumptions for the emissions are different in the two MIPs. The similarity indicates scenarios of τ could be assessed against observational data and used as an analog story for climate studies, even in some cases of unexpected emission changes that are not foreseen at the time of the production of emission projections.

FIEDLER ET AL. 11 of 22

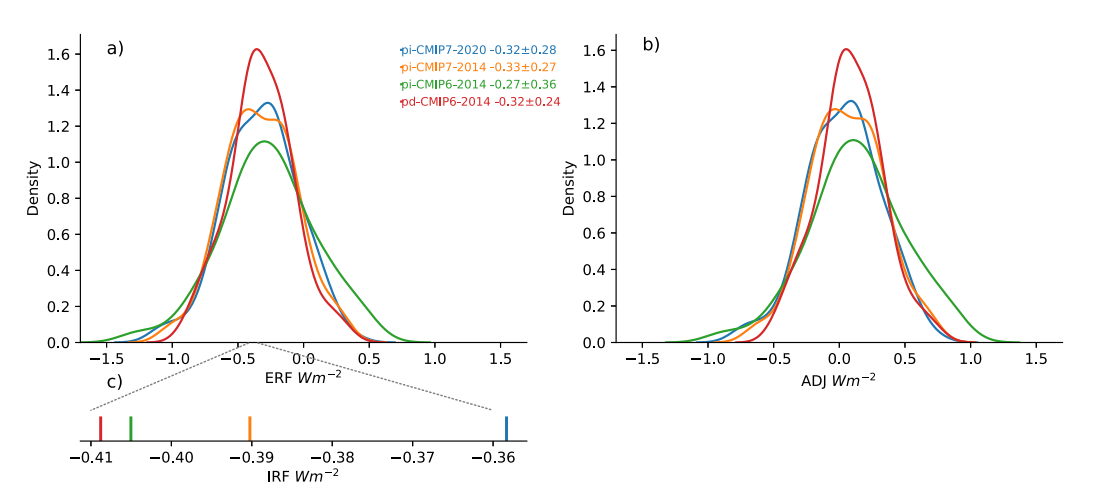


Figure 6. Distribution of annual averages of anthropogenic aerosol forcing. Shown are the density distributions of globally and annually averaged (a) effective radiative forcing (ERF_{all}) and (b) net contributions from rapid adjustments (ADJ_{all}) . The zoom in the x-axis (c) shows the 30-year mean of the global instantaneous radiative forcing (IRF_{all}) . All values are for all-sky conditions for present-day aerosol patterns and calculated for shortwave radiation at the top of the atmosphere from the color-coded ICON-N atmosphere-only experiments, listed in Table 1 as piClim-X and pdClim-X where X refers to the different climate forcings data. The mean and year-to-year standard deviation of ERF_{all} are listed in the legend of (a). See Section 2.3.1 for method description.

3.2. Radiative Forcing

3.2.1. Emission Dependency

We estimate an effective radiative forcing for all sky conditions (ERF_{all}) of about -0.33 Wm^{-2} for the 2014 anthropogenic aerosols relative to the pre-industrial (1850) aerosol from SPv2 in ICON-NWP. The ERF_{all} from SPv2 is slightly more negative by -0.06 Wm^{-2} compared to SPv1 for the 2014 aerosols and changes little by 0.01 Wm⁻² for 2020 (Figure 6a). ERF are computed for shortwave radiation at the top of the atmosphere from piClim experiments with ICON-NWP (Section 2.3.1). The SPv2 to SPv1 differences in present-day ERF_{all} are small compared to the model internal variability in the shortwave radiation budget at the top of the atmosphere, measured with year-to-year standard deviations of 0.24–0.36 Wm⁻² in all-sky conditions (Figure 6a). Year-to-year differences in ERF_{all} are explained by variability in the net contribution of rapid adjustments in the atmosphere (Figure 6b), since the instantaneous radiative forcing is stable within a few years after spin-up (Figure 6c).

ICON's ERF_{all} of anthropogenic aerosols for 2014 of -0.33 Wm^{-2} falls at the upper end of other lines of evidence and is weaker compared to estimates from CMIP6 models. For instance, models participating in CMIP6 had a range in ERF_{all} of about -1.4 to -0.6 Wm^{-2} (C. J. Smith et al., 2020). Other models using the 2014 anthropogenic aerosol from SPv1 have more negative ERF_{all} of -0.79 to -0.46 Wm^{-2} (Fiedler et al., 2023) compared to ICON-NWP. The ERF_{all} of ICON-NWP is, however, near the margin of the 10%–90% confidence level for ERF_{all} of -2.0 to -0.4 Wm^{-2} , assessed from multiple lines of evidence by Bellouin et al. (2020), and within the range of $-1.0 \text{ to } -0.3 \text{ Wm}^{-2}$ suggested by Stevens (2015).

Clouds in ICON-NWP more strongly mask ERF compared to MPI-ESM1.2, consistent with the weaker ERF_{all}. Clouds can mask ERF_{clear}, reducing the global magnitude of ERF_{all} (Fiedler et al., 2017). ICON-NWP has a global mean ERF_{clear} of about -0.8 Wm^{-2} with regional values of around -9 Wm^{-2} for present-day aerosol from SPv1 and SPv2 (Figures 7b and 7e). Global mean ERF_{clear} in ICON-NWP is more negative than global mean ERF_{clear} in the atmosphere component of the CMIP6 model MPI-ESM1.2 (Fiedler et al., 2017), yet the ERF_{all} in ICON-NWP is less negative. It suggests that the influence of cloud masking on ERF_{all} in ICON-NWP is approximately three times stronger, namely $+0.55 \text{ Wm}^{-2}$ (ERF_{all} minus ERF_{clear} for pi-CMIP6-2014), compared to $+0.17 \text{ Wm}^{-2}$ from SPv1 in MPI-ESM1.2 (Fiedler et al., 2017).

We test to what extent global mean ERF_{all} and regional effective radiative effects differ between SPv1 and SPv2 when we use a substantially different global pattern of anthropogenic aerosol. We compare the effective radiative

FIEDLER ET AL. 12 of 22

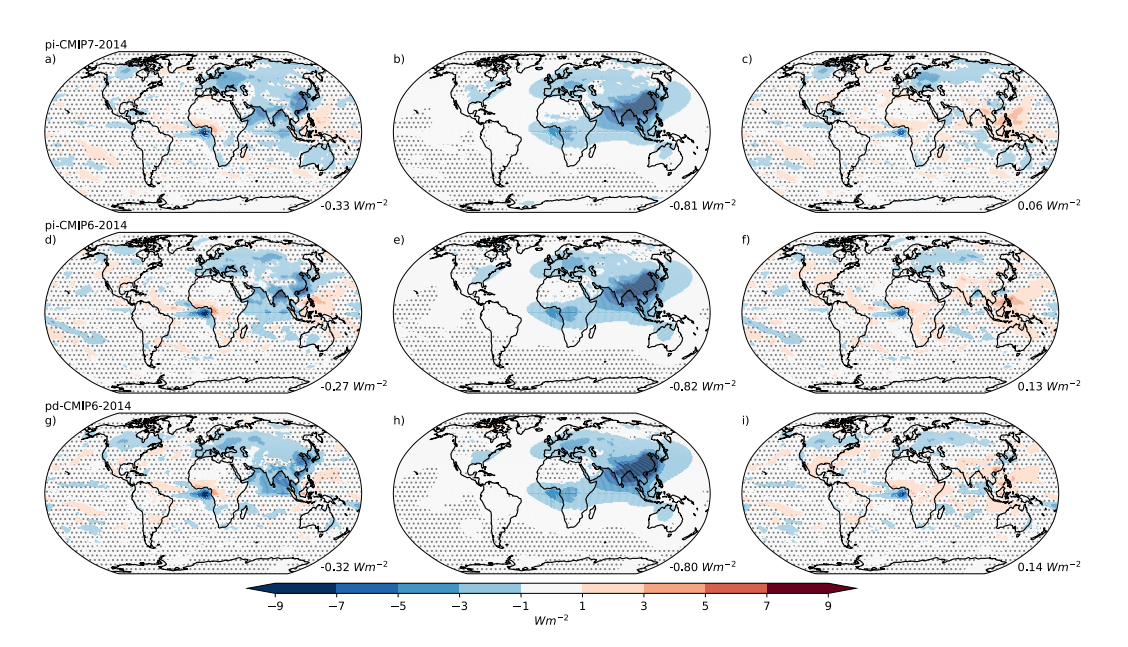


Figure 7. Radiative effects of anthropogenic aerosol forcing of 2014. Shown are the regional contributions to (left to right) all-sky effective radiative forcing (ERF_{clear}), clear-sky effective radiative forcing (ERF_{clear}), and all-sky net contributions of rapid adjustments (ADJ_{all}). All values are for all-sky conditions in 2014 and calculated for shortwave radiation at the top of the atmosphere from the ICON-NWP experiments (top to bottom) pi-CMIP7-2014, pi-CMIP6-2014, and pd-CMIP6-2014 (Table 1). Hatching indicates results not significant at the 95% level using a standard t-test. Values in the lower right corners are the global means.

effects from piClim experiments for the mid-1970s anthropogenic aerosols (Figure S4 in Supporting Information S1), when most of the aerosol was over North America and Europe (Figure 1), against results for the present-day aerosol maxima in East Asia in 2014 and 2020. The global mean ERF_{all} are similar for the 1975, 2014, and 2020 aerosol with global mean differences of less than 0.09 Wm⁻², despite strong regional differences in the effective radiative effects (compare Figure 7a and Figure S4d in Supporting Information S1). The small influence of the substantial change in aerosol patterns is consistent with ERF_{all} of the mid-1970s and the mid-2000s in other models (Fiedler, Kinne, et al., 2019). It implies the 1970–2020s changes in the regional aerosol emissions had moderate influence on the anthropogenic aerosol forcing in ICON-NWP, consistent with the small trend in ERF_{all} of anthropogenic aerosols for 2000–2014 in the CMIP6 multi-model ensemble mean of historical experiments (Fiedler et al., 2023). ICON-NWP adjusts differently to the mid-1970s and mid-2010s aerosol patterns of SPv1 and SPv2, although these differences are small in the global mean compared to the internal variability in the shortwave radiation budget (Supporting Information S1). Specifically, the differences in ADJ_{all} for the two aerosol patterns are about half of the year-to-year standard deviation in the global mean radiation budget, and fall within the model-to-model difference for ADJ_{all} = [0.03; 0.2] Wm⁻² from an earlier intercomparison study (Fiedler, Kinne, et al., 2019).

3.2.2. Base State Dependency

The climate base state has little influence on the present-day effective radiative effects of anthropogenic aerosols in ICON-NWP. We test the influence of the base state for SPv1 in what we call pdClim experiments. The pdClim experiments are similar to piClim but have a prescribed present-day climatology of sea-surface temperatures and sea ice (Section 2.3.1). The different sea-surface conditions between the pre-industrial and present-day lead to notable changes in the mean climate, namely global warming and associated changes in clouds, precipitation and wind patterns (Figure S5 in Supporting Information S1).

Using the substantially different base climates causes a comparable small difference in global mean ERF_{all} of the 2014 anthropogenic aerosol. Global mean ERF_{all} for the 2014 aerosol changes by 0.05 Wm⁻² with the different base state (Figure 6). That difference in the global mean ERF_{all} due to the base state is for instance similar to the estimated difference in ERF_{all} for 2014 between SPv1 to SPv2 (Figure 6).

FIEDLER ET AL. 13 of 22

Moreover, the regional patterns of effective radiative effect and net contributions from rapid adjustments to the anthropogenic aerosol of 2014 are broadly similar from piClim and pdClim with some perceptual differences over North America, in Europe, and around the Maritime continent (Figures 7f and 7i). Clouds, precipitation and wind patterns change with a warmer base state (Figure S5 in Supporting Information S1). Anthropogenic aerosols from SP directly influence the radiative transfer in the atmosphere through scattering and absorption of shortwave radiation, and perturb the cloud droplet number concentration affecting the simulated cloud albedo in ICON-NWP. Such aerosol effects influence the vertical temperature profiles and therefore clouds and precipitation in the model. Nevertheless, the different base states as in pdClim and piClim yield similar spatial patterns for the effective radiative effects of the 2014 aerosols (Figures 7d and 7g). This result suggests a weak sensitivity of the anthropogenic aerosol forcing and net contributions from rapid adjustments to the pre-industrial to present-day climate change in ICON-NWP. Other models could show different results, for example, when they simulate additional processes for aerosol and atmospheric chemistry that consider adjustments of the aerosol emission and deposition fluxes.

3.3. Climate Response

3.3.1. Global Mean

Two three-member ensembles of historical experiments with ICON XPP are performed for the anthropogenic aerosols from SPv1 (hist-CMIP6) and SPv2 (hist-CMIP7), which are identical in all other aspects of the experimental setup (see Section 2.3.2, Table 2). A comparison of the ICON XPP output against observational reference data sets and CMIP6 model results allows us to evaluate the climate response to the updated SPv2 against SPv1 data. We document the performance of ICON XPP for selected variables and identified responses to regional aerosol changes that have been seen in other climate models.

The global mean outgoing shortwave radiation at the top of the atmosphere (RSUT) in ICON XPP falls at the upper end of most individual simulations from CMIP6 models, although not at the upper end of the entire CMIP6 model ensemble (compare against gray lines in Figure 8a). There are no notable differences between hist-CMIP6 and hist-CMIP7 (Figure 8a). Mean RSUT from the historical experiments agrees well with MERRA2 (not shown) and ISCCP-FH, and is overestimated compared to CERES EBAF with a mean bias of 4.5 Wm⁻². ICON XPP also reproduces the sharp increases in mean RSUT after major volcanic eruptions, for example, Pinatubo and Krakatoa to name the two largest natural anomalies in RSUT during the historical period.

There is no notable difference in the global mean near-surface air temperature (T_{2m}) between hist-CMIP6 and hist-CMIP7 (Figure 8b), although individual members follow slightly different trajectories for T_{2m} associated with the simulated internal variability in ICON XPP. All historical experiments of ICON XPP successfully reproduce the observed increase in T_{2m} from observational data and are close to the observed T_{2m} of HadCRUT5 for 1979–2020 with a mean bias of 0.005 K. The global mean T_{2m} from ICON XPP falls in the middle of the CMIP6 ensemble spread for the entire historical period.

Global mean precipitation (p) from ICON XPP falls at the upper end of the CMIP6 multi-model spread with again similar results for hist-CMIP6 and hist-CMIP7 (Figure 8c). ICON XPP has a global mean p of about 3.15 mm day⁻¹ and a slight increase in p toward the 21st century, consistent with the temperature increase. Compared to ERA5 and GPCP-SG, the multi-member ensemble mean of ICON XPP overestimates p with a global mean bias of 0.49 mm day⁻¹ for 1979–2020.

3.3.2. Spatial Pattern

We assess the spatial pattern of the mean differences in the top of atmosphere outgoing shortwave radiation (RSUT) from SPv2 between the mean for 1960–1979 against the pre-industrial and for 2000–2019 against 1960–1979 (Figures 9a and 9b), which are affected by substantially different spatial patterns of anthropogenic aerosol (Section 3.2). In many regions, the aerosol effective radiative effects, that imply increasing RSUT, are overcompensated by responses leading to a reduction in RSUT. The responses are strong enough to cause regional reductions of RSUT of up to $6~\rm Wm^{-2}$, for example, in parts of North America for the 1960–1979 mean relative to the pre-industrial. Most pronounced increases in RSUT of 2–6 Wm⁻² are seen over oceans in the tropics and around Europe for the 1960–1979 mean relative to the pre-industrial state (Figure 9a), and around East Asia for the 2000–2019 mean against 1960–1979 (Figure 9b).

FIEDLER ET AL. 14 of 22

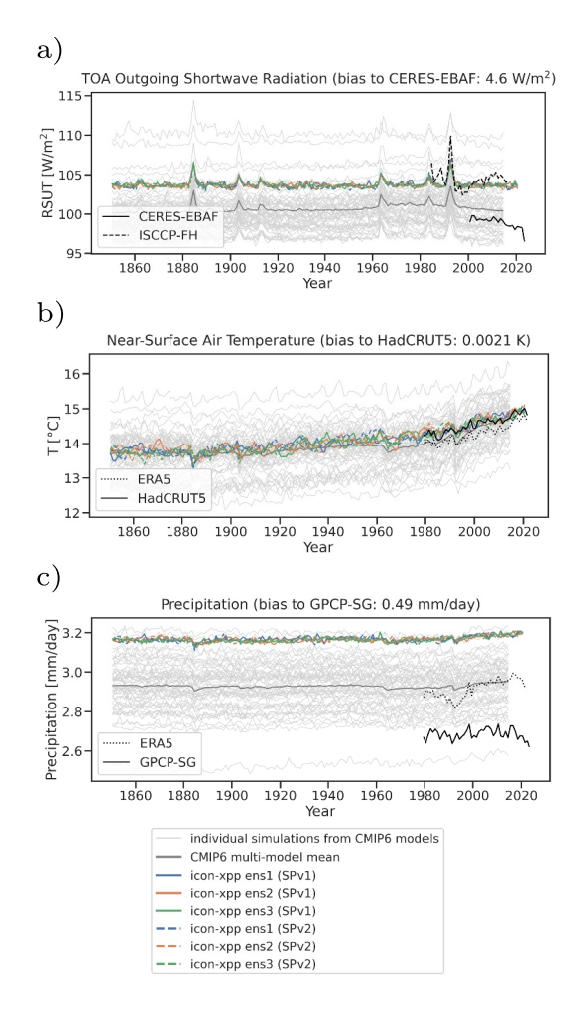


Figure 8. Historical changes in global mean climate. Shown are (a) outgoing shortwave radiation at the top of the atmosphere, (b) near-surface air temperature, and (c) precipitation for 1850–2020 based on fully-coupled historical experiments with ICON XPP and CMIP6 models, and observational data, listed in Tables 2 and 3. Solid and dashed colored lines show ICON XPP experiments with anthropogenic aerosols from SPv1 (hist-CMIP6) and SPv2 (hist-CMIP7), respectively. Numbers in brackets in the titles are the global mean bias of the ICON XPP mean over all ensemble members relative to the corresponding observational data set (averaged over the time period spanned by maximum overlap between ICON XPP and the corresponding observational data set, see Table 3). Gray lines are (thin) individual historical experiments from CMIP6 and (thick) the multi-model mean from all CMIP6 historical experiments with equal weighting of the contributing models.

The changes in RSUT over time are often an order of magnitude smaller than regional biases computed for the present-day mean RSUT from the CERES-EBAF and ISCCP-FH observational data (Figures 10a and 10b), although the present-day anthropogenic aerosol from SPv2 helps to slightly reduce the positive bias in RSUT around the Maritime continent and Australia by –1 to –3 Wm⁻² compared to SPv1 (not shown). We see for instance biases of around 40 Wm⁻² in the tropics with an underestimation in ICON XPP over coastal upwelling regions and an overestimation in ocean regions to the West (Figures 10a and 10b). The agreement in the global mean RSUT between ICON XPP and ISCCP-FH (Figure 8a) is therefore due to regional biases of different signs that compensate each other in the global mean with overall minor differences induced by SPv2 against SPv1.

The response pattern of T_{2m} to climate forcings in ICON XPP is again similar with SPv2 and SPv1 with a continuous warming that is stronger in the northern than in the southern hemisphere and particularly pronounced over the Arctic (response with SPv2 shown in Figures 9c and 9d). Maximum regional differences of T_{2m} are -0.5 K in hist-CMIP7 compared to hist-CMIP6 for 2001-2019 in northern parts of North America and Asia, where SPv2 leads to slightly less present-day regional warming compared to SPv1 (not shown). SPv2 therefore helps to slightly reduce the present-day warm bias over North America, seen for hist-CMIP7 against both ERA5 and HadCRUT5 (Figures 10c and 10d). Moreover, near-surface air over coastal upwelling regions, for example, offshore of the coast of Southwest Africa and South America, is up to 4 K too warm with coinciding underestimation of RSUT by ICON XPP (Figures 10c and 10d) and too low total cloudiness (Figures 10g and 10h). It suggests too little scattering of shortwave radiation by the here typically prevailing low stratocumulus clouds in ICON XPP. Many land regions warm in comparison to observational data too little, for example, Africa, and large parts of Asia. Close agreement in the global mean T_{2m} of ICON XPP with observational data are therefore also due to compensating regional biases of the simulated warming (Figure 8b) without noticeable differences with SPv2 against SPv1.

Tropical precipitation for 2002–2019 from ICON XPP shows a pattern of biases relative to ERA5 and GPCP-SG (Figures 10e and 10f) that is broadly similar to biases identified for the multi-model mean of CMIP6 compared to TRMM observation (Fiedler et al., 2020). This includes for instance the dipole of over- and underestimation over the tropical Atlantic. Compared to the regional biases of up to ± 6 mm day⁻¹, differences between SPv2 and SPv1 are again an order of magnitude smaller (not shown) and help to reduce biases only in some regions. Over the ocean around the Maritime continent, SPv2 helps to reduce for instance the regional wet bias of up to -0.75 mm day⁻¹ compared to SPv1 (not shown). Historical changes in precipitation

patterns like the reduced rain over the Sahel in the 1960–1980s and the subsequent wetter conditions (Zhang & Steiner, 2022) are not simulated by ICON XPP (Figures 9e and 9f). Taken together, the simulated rain in ICON XPP is overestimated in more regions than it is underestimated, particularly over the oceans, which explains the positive bias in the simulated global mean precipitation (Figure 8c).

4. Discussion

The here-presented update and extension of the historical data for the simple plumes parameterization for 1850–2020 shows little difference for the anthropogenic aerosol optical depth and effects on cloud droplets, compared to the aerosol variant for 1850–2014 produced for use in CMIP6 (Stevens et al., 2017). Testing the two aerosol variants in historical experiments with the new CMIP7 climate model ICON XPP yields similar global mean

FIEDLER ET AL. 15 of 22

19422466, 2025, 10, Downloaded from https://agupubs.onlinelibrary.wiley.com/doi/10.1029/2025MS00567 by Dxeh Zertrum F. Luft-U. Raum Fahrt n.D. Helmholtz Genien, Wiley Online Library on [24/10/2025], See the Terms and Conditions (https://onlinelibrary.wiley.com/term)

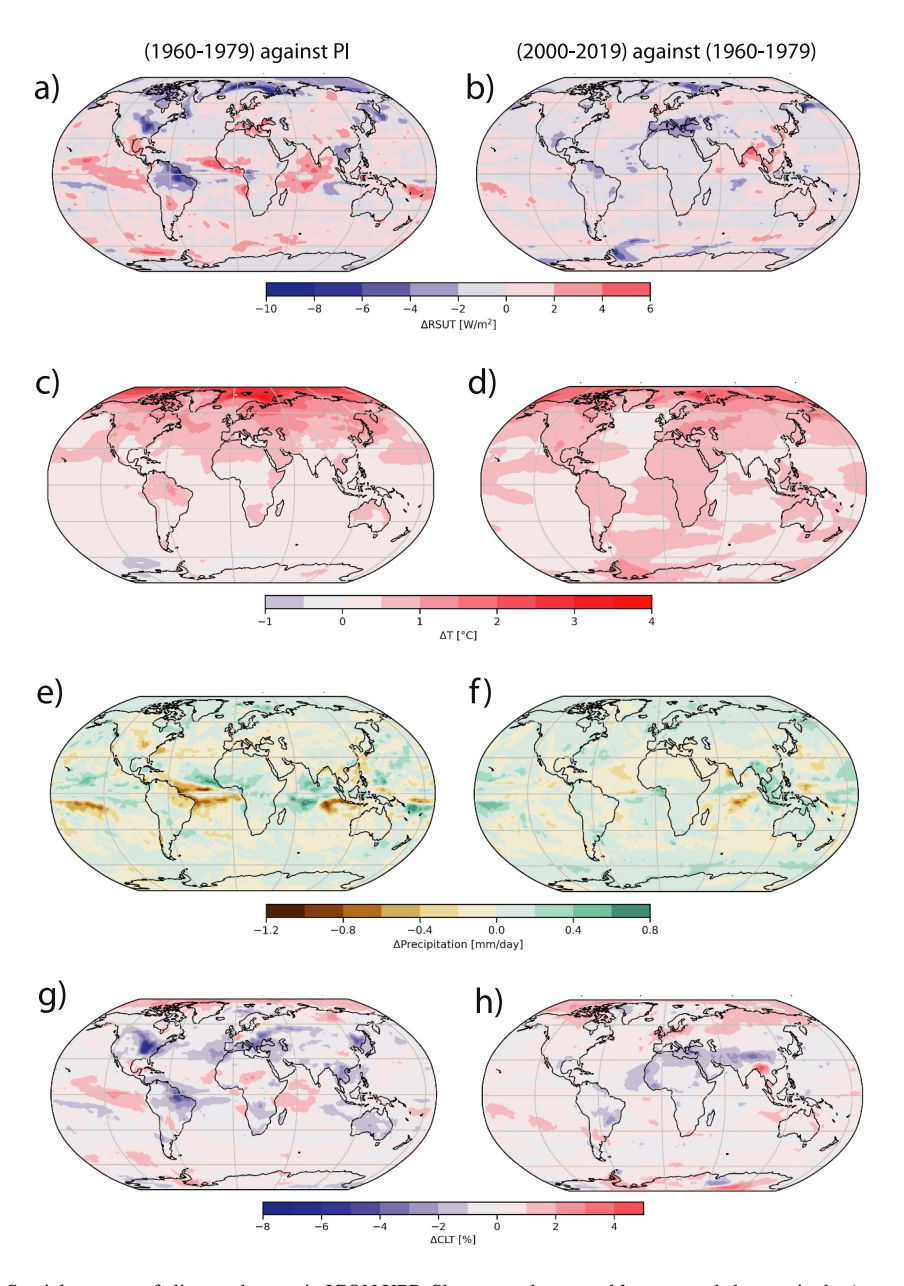


Figure 9. Spatial patterns of climate changes in ICON XPP. Shown are the ensemble-averaged changes in the (top to bottom) outgoing shortwave radiation at the top of the atmosphere, near-surface air temperature, total precipitation, and total cloud cover for (left) the mean of 1960–1979 against the pre-industrial state, and (right) the mean of 2000–2019 against 1960–1979. All data are from ICON XPP historical experiments with SPv2 aerosol data (hist-CMIP7) as described in Section 2.3.2.

radiative forcing and climate responses for anthropogenic aerosols. One example are aerosol-induced differences for ERF that fall within the year-to-year natural variability in the shortwave radiation budget. Induced differences in the global mean response for temperature and precipitation are an order of magnitude smaller compared to the multi-model spread of CMIP6. Assessed globally averaged responses from ICON XPP fall in the middle of the model-to-model differences across the CMIP6 ensemble of historical experiments, although few regionally limited improvements for the simulated present-day climate state are seen in ICON XPP with the updated aerosol data

The similarity for the two aerosol variants for the historical period suggest regularly recurring extensions of previously existing historical data for the simple plumes parameterization is sufficient for climate studies as time progresses. Updates to the entire historical simple plumes data may not be required as long as there are no

FIEDLER ET AL. 16 of 22

19422466, 2025, 10, Downloaded from https://agupubs.onlinelibrary.wiley.com/doi/10.1029/2025MS005067 by Dusch Zentrum F. Luft-U. Raum Flahrt In D. Helmholz Gemein., Wiley Online Library on [24/10/2025]. See the Terms and Conditions (https://onlinelibrary.wiley.

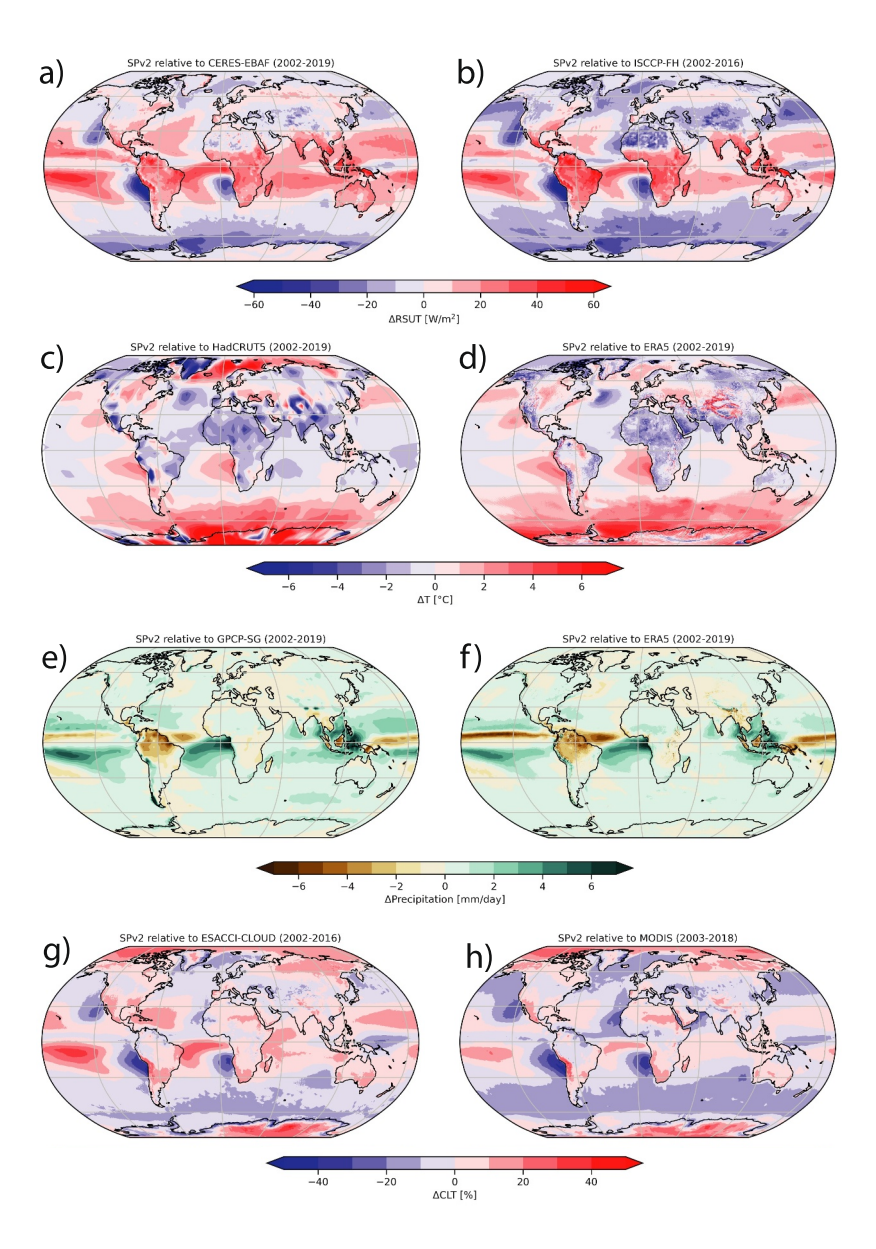


Figure 10. Spatial patterns of biases in ICON XPP. Shown is the ensemble-averaged differences in the (top to bottom) outgoing shortwave radiation at the top of the atmosphere, near-surface air temperature, total precipitation, and total cloud cover as simulated in the historical experiments of ICON XPP with SPv2 (hist-CMIP7) against different observational data sets (Table 3).

substantial revisions to the spatial and temporal distribution of emissions of SO₂ and NH₃. It is useful to retain the decadal scaling for the data in the simple plumes parameterization for use in CMIP. One reason is the small influence of even drastic year-to-year changes in anthropogenic aerosol emissions in global mean climate simulated by CMIP-class models as seen in CovidMIP (Jones et al., 2021). The assessment of the spatial patterns of trends in anthropogenic aerosol optical depth from the CMIP6 variant of SP over the past years further suggested a regular observation-based comparison of scenarios for extending the historical SP data might be useful for climate predictions, even when no annual extension of historical emissions is available in time. The CMIP7 data for the simple plumes aerosol forcing will be generated for all scenarios proposed for ScenarioMIP-CMIP7 (van Vuuren et al., 2025) and variants of these scenarios for AerChemMIP2 (Fiedler et al., n.d.). Depending on the application, other needs for the temporal resolution and coverage of aerosol forcing might be identified keeping the assumptions for the design of the parameterization in mind (Stevens et al., 2017).

FIEDLER ET AL. 17 of 22

An interesting result from our study is the small all-sky ERF for the present-day anthropogenic aerosol of -0.33Wm⁻² for the new CMIP model ICON XPP (Müller, Lorenz, et al., 2025), compared to CMIP6 model estimates (C. J. Smith et al., 2020). At the same time, the model simulates about -0.8 Wm⁻² aerosol ERF for clear sky, which is more negative than the lower bound of $-0.58 \, \mathrm{Wm^{-2}}$ assessed by Bellouin et al. (2020). The small all-sky ERF is due to an about three times larger reduction of clear-sky aerosol ERF due to cloud masking, compared to the CMIP6 model MPI-ESM1.2 with the same simple plumes parameterization (Fiedler et al., 2017). The dependence of aerosol ERF on the climate state and the 2014 to 2020 change of anthropogenic aerosols are comparably small in ICON XPP. ICON XPP (Müller, Früh, et al., 2025) has several new parameterization schemes and a different dynamical core compared to MPI-ESM1.2 (Mauritsen et al., 2019). For instance, the cloud cover was based on threshold-dependent values for the relative humidity following Sundqvist et al. (1989) in MPI-ESM1.2, whereas ICON XPP diagnoses cloud cover following the description from Prill et al. (2024). Moreover, the radiative transfer calculations differ between the two models, namely the ecRad radiation parameterization (Hogan & Bozzo, 2018) is used in ICON XPP whereas MPI-ESM1.2 used the PSrad implementation of RRTMG (Pincus & Stevens, 2013). It will be interesting to investigate the sensitivity of the aerosol ERF in ICON XPP with the newly available parameterization schemes in future studies and revisit the multimodel spread of aerosol ERF including the new CMIP7 models like ICON XPP.

5. Conclusion

We have updated and extended the SP data for 1850–2020 in SPv2 (Fiedler & Sudarchikova, 2024). Differences of SPv2 compared to the CMIP6 data variant SPv1 (Stevens et al., 2017) are small, documented here for the aerosol optical depth, the radiative forcing and the climate response in the new CMIP7 model ICON XPP. The newly available CMIP7 forcing data set SPv2.1 for 1850–2023 is virtually identical to SPv2 for the overlapping period 1850–2020, documented and available from Fiedler and Azoulay (2025). It suggests future extensions of SP historical data, rather than an update of the entire time series of SP data for the past, will be sufficiently accurate for some climate studies, unless the spatial patterns of aerosol and their precursor emissions or other assumptions of the simple plumes parameterization (Stevens et al., 2017) will be revised.

We found that the present-day effective radiative forcing of anthropogenic aerosols from both SPv1 and SPv2 with about -0.3 Wm^{-2} from the atmospheric model component of the new CMIP7 model ICON XPP (Müller, Lorenz, et al., 2025) is less negative compared to estimates from CMIP6 and other lines of evidence. It is therefore no surprise that climate responses with SPv2 and SPv1 yield similar results in the fully coupled historical experiments shown here. Aerosol effects on clouds remain a key uncertainty in the understanding of climate change (Bellouin et al., 2020). Their magnitude in the simple plumes parameterization can be changed in the future for experimentation following existing strategies (Fiedler et al., 2017) or in future variants of SP data for use in the multiple different applications of SP in climate sciences.

Global Research Collaboration Statement

We thank Vaishali Naik, Paul Durack, and Zebedee Nicholls from the CMIP Climate Forcing Task Team, and Eleanor O'Rourke from the CMIP IPO for their coordination and support in the preparation and dissemination of the CMIP climate forcings data sets. We thank our early adopters at the German Weather Service (DWD) and the European Centre for Medium-Range Weather Forecasting (ECMWF) for testing SP data in their model systems for CMIP7-like historical experiments, for climate predictions, and for satellite retrievals.

Conflict of Interest

The authors declare no conflicts of interest relevant to this study.

Data Availability Statement

The data file for Simples Plumes SPv2 for 1850–2020 is available on zenodo (Fiedler & Sudarchikova, 2024) and the code of the simple plumes parameterization and SPv1 for 1850–2014 is available from Stevens et al. (2017). The ICON model code is available online (ICON partnership (DWD and MPI-M and DKRZ and KIT and C2SM), 2024). Source code for reproducing Figures 8–10 with ESMValTool (Andela et al., 2024b) and its core dependency ESMValCore (Andela et al., 2024a) is publicly available on Zenodo (Schlund, 2025). ERA5 data

FIEDLER ET AL. 18 of 22

19422466, 2025, 10, Downloaded

Gemein., Wiley Online Library on [24/10/2025]. See the Ter

(Hersbach et al., 2020) was downloaded from the Copernicus Climate Change Service (2019). The results contain modified Copernicus Climate Change Service information 2025. Neither the European Commission nor ECMWF is responsible for any use that may be made of the Copernicus information or data it contains. CMIP6 data required to reproduce the analyses of this paper is available through the Earth System Grid Foundation (ESGF; https://esgf-metagrid.cloud.dkrz.de/search/cmip6-dkrz/, last access: 19 February 2025). ESMValTool can automatically download these data if requested (see https://docs.esmvaltool.org/projects/ESMValCore/en/v2.11.1/quickstart/configure.html#esgf-configuration, last access: 19 February 2025). Observational/reanalysis data sets are not distributed with ESMValTool that is restricted to the code as open source software, but ESMValTool provides a collection of scripts with downloading and processing instructions to recreate the observational/reanalysis data used for Figures 8–10 (see https://docs.esmvaltool.org/en/latest/input.html/#observations, last access: 19 February 2025). Output from ICON XPP experiments is available from Wahl and Fiedler (2025).

Acknowledgments

SF was supported by the Horizon Europe project EXPECT (Towards an Integrated Capability to Explain and Predict Regional Climate Changes) under Grant Agreement 101137656 and by the Deutsche Forschungsgemeinschaft (DFG, German Research Foundation)-SFB 1502/1-2022project number 450058266. This work used resources of the Deutsches Klimarechenzentrum (DKRZ) granted by its Scientific Steering Committee (WLA) to SF under project ID bb1198 for the forcing generation, performing ICON experiments, data analyses and data publication for this manuscript. MS received funding from the BMBF under CAP7 project, Grant Agreement No. 01LP2401C. We thank Vaishali Naik for reviewing an earlier version of this manuscript and Steve Smith for providing information on differences between CEDS data releases. We acknowledge the funding share of the University Heidelberg for covering the publication fee. Open Access funding enabled and organized by Projekt DEAL.

References

- Adler, R., Wang, J.-J., Sapiano, M., Huffman, G., Chiu, L., Xie, P.-P., et al. NOAA CDR Program. (2017). Global precipitation climatology project (GPCP) climate data record (CDR), version 2.3 (monthly). NOAA National Centers for Environmental Information. https://doi.org/10.7289/V56971M6
- Andela, B., Broetz, B., de Mora, L., Drost, N., Eyring, V., Koldunov, N., et al. (2024a). ESMValCore. Zenodo. https://doi.org/10.5281/zenodo. 3387139
- Andela, B., Broetz, B., de Mora, L., Drost, N., Eyring, V., Koldunov, N., et al. (2024b). ESMValTool. Zenodo. https://doi.org/10.5281/zenodo.
- Bellouin, N., Quaas, J., Gryspeerdt, E., Kinne, S., Stier, P., Watson-Parris, D., et al. (2020). Bounding global aerosol radiative forcing of climate change. *Reviews of Geophysics*, 58(1), e2019RG000660. https://doi.org/10.1029/2019RG000660
- Chen, C., Dubovik, O., Fuertes, D., Litvinov, P., Lapyonok, T., Lopatin, A., et al. (2020). Validation of grasp algorithm product from POLDER/PARASOL data and assessment of multi-angular polarimetry potential for aerosol monitoring. *Earth System Science Data*, 12(4), 3573–3620. https://doi.org/10.5194/essd-12-3573-2020
- Cherian, R., & Quaas, J. (2020). Trends in aod, clouds, and cloud radiative effects in satellite data and CMIP5 and CMIP6 model simulations over aerosol source regions. *Geophysical Research Letters*, 47(9), e2020GL087132. https://doi.org/10.1029/2020GL087132
- Copernicus Climate Change Service. (2019). ERA5 monthly averaged data on single levels from 1940 to present. Copernicus Climate Change Service (C3S) Climate Data Store (CDS). https://doi.org/10.24381/CDS.F17050D7
- Dunne, J. P., Hewitt, H. T., Arblaster, J., Bonou, F., Boucher, O., Cavazos, T., et al. (2024). An evolving coupled model intercomparison project phase 7 (CMIP7) and fast track in support of future climate assessment. EGUsphere, 2024, 1–51. https://doi.org/10.5194/egusphere-2024-3874
- Eyring, V., Bony, S., Meehl, G. A., Senior, C. A., Stevens, B., Stouffer, R. J., & Taylor, K. E. (2016). Overview of the Coupled Model Inter-comparison Project Phase 6 (CMIP6) experimental design and organization. Geoscientific Model Development, 9(5), 1937–1958. https://doi.org/10.5194/gmd-9-1937-2016
- Fiedler, S., O'Connor, F. M., Watson-Parris, D., Allen, R. J., Griffith, P., Kasoar, M., et al. (n.d.). AerChemMIP phase 2: Unraveling the role of reactive gases and aerosols for air quality, climate responses and feedbacks. (in prep.).
- Fiedler, S., & Azoulay, A. (2025). CMIP7 climate forcings dataset: Simple plumes for anthropogenic aerosols. Zenodo. https://doi.org/10.5281/
- Fiedler, S., Crueger, T., D'Agostino, R., Peters, K., Becker, T., Leutwyler, D., et al. (2020). Simulated tropical precipitation assessed across three major phases of the Coupled Model Intercomparison Project (CMIP). *Monthly Weather Review*, 148(9), 3653–3680. https://doi.org/10.1175/MWR-D-19-0404.1
- Fiedler, S., Kinne, S., Huang, W. T. K., Räisänen, P., O'Donnell, D., Bellouin, N., et al. (2019). Anthropogenic aerosol forcing Insights from multiple estimates from aerosol-climate models with reduced complexity. Atmospheric Chemistry and Physics, 19(10), 6821–6841. https://doi.org/10.5194/acp-19-6821-2019
- Fiedler, S., Naik, V., O'Connor, F. M., Smith, C. J., Griffiths, P., Kramer, R. J., et al. (2024). Interactions between atmospheric composition and climate change Progress in understanding and future opportunities from AerChemMIP, PDRMIP, and RFMIP. Geoscientific Model Development, 17(6), 2387–2417. https://doi.org/10.5194/gmd-17-2387-2024
- Fiedler, S., & Putrasahan, D. (2021). How does the North Atlantic SST pattern respond to anthropogenic aerosols in the 1970s and 2000s? Geophysical Research Letters, 48(7), e2020GL092142. https://doi.org/10.1029/2020gl092142
- Fiedler, S., Stevens, B., Gidden, M., Smith, S. J., Riahi, K., & van Vuuren, D. (2019). First forcing estimates from the future CMIP6 scenarios of anthropogenic aerosol optical properties and an associated Twomey effect. Geoscientific Model Development, 12(3), 989–1007. https://doi.org/ 10.5194/gmd-12-989-2019
- Fiedler, S., Stevens, B., & Mauritsen, T. (2017). On the sensitivity of anthropogenic aerosol forcing to model-internal variability and parameterizing a Twomey effect. *Journal of Advances in Modeling Earth Systems*, 9(2), 1325–1341. https://doi.org/10.1002/2017MS000932
- Fiedler, S., & Sudarchikova, N. (2024). CMIP climate forcings dataset: Simple plumes for anthropogenic aerosols. Zenodo. https://doi.org/10.5281/zenodo.14512962
- Fiedler, S., van Noije, T., Smith, C. J., Boucher, O., Dufresne, J.-L., Kirkevåg, A., et al. (2023). Historical changes and reasons for model differences in anthropogenic aerosol forcing in CMIP6. *Geophysical Research Letters*, 50(15), e2023GL104848. https://doi.org/10.1029/2023GL104848
- Fiedler, S., Wyser, K., Rogelj, J., & van Noije, T. (2021). Radiative effects of reduced aerosol emissions during the COVID-19 pandemic and the future recovery. *Atmospheric Research*, 264, 105866. https://doi.org/10.1016/j.atmosres.2021.105866
- Fioletov, V. E., McLinden, C. A., Griffin, D., Abboud, I., Krotkov, N., Leonard, P. J. T., et al. (2023). Version 2 of the global catalogue of large anthropogenic and volcanic SO₂ sources and emissions derived from satellite measurements. *Earth System Science Data*, 15(1), 75–93. https://doi.org/10.5194/essd-15-75-2023
- Forster, P. M., Richardson, T., Maycock, A. C., Smith, C. J., Samset, B. H., Myhre, G., et al. (2016). Recommendations for diagnosing effective radiative forcing from climate models for CMIP6. *Journal of Geophysical Research*, 121(20), 12460–12475. https://doi.org/10.1002/2016ID025320

FIEDLER ET AL. 19 of 22

Wiley Online Library on [24/10/2025].

- Gelaro, R., McCarty, W., Suárez, M. J., Todling, R., Molod, A., Takacs, L., et al. (2017). The modern-era retrospective analysis for research and applications, version 2 (MERRA-2). *Journal of Climate*, 30(14), 5419–5454. https://doi.org/10.1175/JCLI-D-16-0758.1
- Gidden, M. J., Riahi, K., Smith, S. J., Fujimori, S., Luderer, G., Kriegler, E., et al. (2019). Global emissions pathways under different socio-economic scenarios for use in CMIP6: A dataset of harmonized emissions trajectories through the end of the century. Geoscientific Model Development, 12(4), 1443–1475. https://doi.org/10.5194/gmd-12-1443-2019
- Giorgetta, M. A., Brokopf, R., Crueger, T., Esch, M., Fiedler, S., Helmert, J., et al. (2018). ICON-A, the atmosphere component of the icon Earth system model: I. Model description. *Journal of Advances in Modeling Earth Systems*, 10(7), 1613–1637. https://doi.org/10.1029/2017MS001242
- Gliß, J., Mortier, A., Schulz, M., Andrews, E., Balkanski, Y., Bauer, S. E., et al. (2021). AeroCom phase iii multi-model evaluation of the aerosol life cycle and optical properties using ground- and space-based remote sensing as well as surface in situ observations. Atmospheric Chemistry and Physics, 21(1), 87–128. https://doi.org/10.5194/acp-21-87-2021
- Gupta, G., Venkat Ratnam, M., Madhavan, B., & Narayanamurthy, C. (2022). Long-term trends in aerosol optical depth obtained across the globe using multi-satellite measurements. *Atmospheric Environment*, 273, 118953. https://doi.org/10.1016/j.atmosenv.2022.118953
- Hagemann, S., Ho-Hagemann, H. T., & Hanke, M. (2023). The hydrological discharge model A river runoff component for offline and coupled model applications. Zenodo. https://doi.org/10.5281/zenodo.7890682
- Hersbach, H., Bell, B., Berrisford, P., Hirahara, S., Horányi, A., Muñoz-Sabater, J., et al. (2020). The ERA5 global reanalysis. *Quarterly Journal of the Royal Meteorological Society*, 146(730), 1999–2049. https://doi.org/10.1002/qj.3803
- Hoesly, R., Smith, S. J., Prime, N., Ahsan, H., Suchyta, H., O'Rourke, P., et al. (2024). CEDS v_2024_10_21 release gridded emissions data 0.5 degree, Zenodo, https://doi.org/10.5281/zenodo.13952845
- Hoesly, R. M., Smith, S. J., Feng, L., Klimont, Z., Janssens-Maenhout, G., Pitkanen, T., et al. (2018). Historical (1750–2014) anthropogenic emissions of reactive gases and aerosols from the community emissions data system (CEDS). Geoscientific Model Development, 11(1), 369–408. https://doi.org/10.5194/gmd-11-369-2018
- Hogan, R. J., & Bozzo, A. (2018). A flexible and efficient radiation scheme for the ECMWF model. *Journal of Advances in Modeling Earth Systems*, 10(8), 1990–2008. https://doi.org/10.1029/2018MS001364
- Hsu, N. C., Gautam, R., Sayer, A. M., Bettenhausen, C., Li, C., Jeong, M. J., et al. (2012). Global and regional trends of aerosol optical depth over land and ocean using SEAWIFS measurements from 1997 to 2010. Atmospheric Chemistry and Physics, 12(17), 8037–8053. https://doi.org/10.5194/acp-12-8037-2012
- ICON partnership (DWD and MPI-M and DKRZ and KIT and C2SM). (2024). ICON release 2024.01. World Data Center for Climate (WDCC) at DKRZ. https://doi.org/10.35089/WDCC/IconRelease01
- Inness, A., Ades, M., Agustí-Panareda, A., Barré, J., Benedictow, A., Blechschmidt, A.-M., et al. (2019). The cams reanalysis of atmospheric composition. Atmospheric Chemistry and Physics, 19(6), 3515–3556. https://doi.org/10.5194/acp-19-3515-2019
- Jones, C. D., Hickman, J. E., Rumbold, S. T., Walton, J., Lamboll, R. D., Skeie, R. B., et al. (2021). The climate response to emissions reductions due to COVID-19: Initial results from COVIDMIP. Geophysical Research Letters, 48(8), e2020GL091883. https://doi.org/10.1029/ 2020GL091883
- Kahn, R. A., Gaitley, B. J., Martonchik, J. V., Diner, D. J., Crean, K. A., & Holben, B. (2005). Multiangle imaging spectroradiometer (MISR) global aerosol optical depth validation based on 2 years of coincident aerosol robotic network (AERONET) observations. *Journal of Geophysical Research*, 110(D10). https://doi.org/10.1029/2004JD004706
- Karlsson, K.-G., Stengel, M., Meirink, J. F., Riihelä, A., Trentmann, J., Akkermans, T., et al. (2023). CLARA-A3: The third edition of the AVHRR-based cm SAF climate data record on clouds, radiation and surface albedo covering the period 1979 to 2023. Earth System Science Data, 15(11), 4901–4926. https://doi.org/10.5194/essd-15-4901-2023
- Kinne, S. (2019). The MACV2 aerosol climatology. Tellus B: Chemical and Physical Meteorology, 71(1), 1623639. https://doi.org/10.1080/16000889.2019.1623639
- Kinne, S., O'Donnel, D., Stier, P., Kloster, S., Zhang, K., Schmidt, H., et al. (2013). MAC-v1: A new global aerosol climatology for climate studies. *Journal of Advances in Modeling Earth Systems*, 5(4), 704–740. https://doi.org/10.1002/jame.20035
- Korn, P., Brüggemann, N., Jungclaus, J. H., Lorenz, S., Gutjahr, O., Haak, H., et al. (2022). ICON-O: The ocean component of the icon Earth system model—Global simulation characteristics and local telescoping capability. *Journal of Advances in Modeling Earth Systems*, 14(10), e2021MS002952. https://doi.org/10.1029/2021ms002952
- Lamboll, R. D., Jones, C. D., Skeie, R. B., Fiedler, S., Samset, B. H., Gillett, N. P., et al. (2021). Modifying emissions scenario projections to account for the effects of COVID-19: Protocol for COVIDMIP. Geoscientific Model Development, 14(6), 3683–3695. https://doi.org/10.5194/gmd-14-3683-2021
- Levy, R. C., Remer, L. A., Mattoo, S., Vermote, E. F., & Kaufman, Y. J. (2007). Second-generation operational algorithm: Retrieval of aerosol properties over land from inversion of moderate resolution imaging spectroradiometer spectral reflectance. *Journal of Geophysical Research*, 112(D13). https://doi.org/10.1029/2006JD007811
- Loeb, N. G., Doelling, D. R., Wang, H., Su, W., Nguyen, C., Corbett, J. G., et al. (2018). Clouds and the earth's radiant energy system (CERES) energy balanced and filled (EBAF) top-of-atmosphere (TOA) edition-4.0 data product. *Journal of Climate*, 31(2), 895–918. https://doi.org/10.1175/jcli-d-17-0208.1
- Mauritsen, T., Bader, J., Becker, T., Behrens, J., Bittner, M., Brokopf, R., et al. (2019). Developments in the MPI-M Earth System Model version 1.2 (MPI-ESM1.2) and its response to increasing CO₂. *Journal of Advances in Modeling Earth Systems*, 11(4), 998–1038. https://doi.org/10.1029/2018ms001400
- Michou, M., Nabat, P., Saint-Martin, D., Bock, J., Decharme, B., Mallet, M., et al. (2020). Present-day and historical aerosol and ozone characteristics in CNRM CMIP6 simulations. *Journal of Advances in Modeling Earth Systems*, 12(1), e2019MS001816. https://doi.org/10.1029/2019MS001816
- Morice, C. P., Kennedy, J. J., Rayner, N. A., Winn, J. P., Hogan, E., Killick, R. E., et al. (2021). An updated assessment of near-surface temperature change from 1850: The HadCRUt5 data set. *Journal of Geophysical Research: Atmospheres*, 126(3), e2019JD032361. https://doi.org/10.1029/2019jd032361
- Moutier, W., Bourgeois, Q., Tetzlaff, A., Clerbaux, N., Stöckli, R., Schröder, M., & Hollmann, R. (2024). CM SAF surface radiation and fluxes from METEOSAT first and second generation Edition 1 (landflux ed. 1). Satellite Application Facility on Climate Monitoring (CM SAF). https://doi.org/10.5676/EUM_SAF_CM/SLF_METEOSAT/V001
- Müller, W. A., Früh, B., Korn, P., Potthast, R., Baehr, J., Bettems, J.-M., et al. (2025). ICON: Toward vertically integrated model configurations for numerical weather prediction, climate predictions, and projections. *Bulletin of the American Meteorological Society*, 106(6), E1017–E1031. https://doi.org/10.1175/BAMS-D-24-0042.1

FIEDLER ET AL. 20 of 22

Library on [24/10/2025].

- Müller, W. A., Lorenz, S., Pham, T. V., Schneidereit, A., Brokopf, R., Brovkin, V., et al. (2025). The ICON-based Earth system model for climate predictions and projections (ICON XPP v1.0). EGUsphere, 2025, 1–60. https://doi.org/10.5194/egusphere-2025-2473
- Nordling, K., Korhonen, H., Räisänen, P., Alper, M. E., Uotila, P., O'Donnell, D., & Merikanto, J. (2019). Role of climate model dynamics in estimated climate responses to anthropogenic aerosols. *Atmospheric Chemistry and Physics*, 19(15), 9969–9987. https://doi.org/10.5194/acp-19-9969-2019
- North, P., Briggs, S., Plummer, S., & Settle, J. (1999). Retrieval of land surface bidirectional reflectance and aerosol opacity from ATSR-2 multiangle imagery. *IEEE Transactions on Geoscience and Remote Sensing*, 37(1), 526–537. https://doi.org/10.1109/36.739106
- North, P., Heckel, A., & Pearson, K. (2021). Su-SLSTR ATBD, C3S ref: C3S_d312a_lot5_202103_su_slstr_atbd_v1.12. Retrieved from cds. climate.copernicus.eu
- Pincus, R., Forster, P. M., & Stevens, B. (2016). The Radiative Forcing Model Intercomparison Project (RFMIP): Experimental protocol for CMIP6. Geoscientific Model Development, 9(9), 3447–3460. https://doi.org/10.5194/gmd-9-3447-2016
- Pincus, R., & Stevens, B. (2013). Paths to accuracy for radiation parameterizations in atmospheric models. *Journal of Advances in Modeling Earth Systems*, 5(2), 225–233. https://doi.org/10.1002/jame.20027
- Platnick, S., King, M., Ackerman, S., Menzel, W., Baum, B., Riedi, J., & Frey, R. (2003). The MODIS cloud products: Algorithms and examples from terra. *IEEE Transactions on Geoscience and Remote Sensing*, 41(2), 459–473. https://doi.org/10.1109/TGRS.2002.808301
- Pozzer, A., de Meij, A., Yoon, J., Tost, H., Georgoulias, A. K., & Astitha, M. (2015). And trends during 2001–2010 from observations and model simulations. *Atmospheric Chemistry and Physics*, 15(10), 5521–5535. https://doi.org/10.5194/acp-15-5521-2015
- Prill, F., Reinert, D., Rieger, D., & Zängl, G. (2024). ICON tutorial-working with the ICON model. deutscher wetterdienst, offenbach.
- Rieger, D., Koehler, M., Hogan, R. J., Schäfer, S., Seifert, A., de Lozar, A., & Zängl, G. (2019). ecRad in ICON Details on the implementation and first results (Tech. Rep.). German Weatherservice. https://doi.org/10.5676/DWDpub/nwv/icon004
- Righi, M., Andela, B., Eyring, V., Lauer, A., Predoi, V., Schlund, M., et al. (2020). Earth system model evaluation tool (ESMVALTOOL) v2.0 Technical overview. *Geoscientific Model Development*, 13(3), 1179–1199. https://doi.org/10.5194/gmd-13-1179-2020
- Samset, B. H., Wilcox, L. J., & Allen, R. J. (2024). Broader research efforts and assessments needed to uncover the complex climate effects of regional changes in aerosol emissions. PLOS Climate, 3(10), e0000508. https://doi.org/10.1371/journal.pclm.0000508
- Schilliger, L., Tetzlaff, A., Bourgeois, Q., Correa, L. F., & Wild, M. (2024). An investigation on causes of the detected surface solar radiation brightening in Europe using satellite data. *Journal of Geophysical Research: Atmospheres*, 129(15), e2024JD041101. https://doi.org/10.1029/
- Schlund, M. (2025). Supplementary material for "First analysis of climate forcing and response to updated historical anthropogenic aerosol with the new CMIP7 model ICON XPP". Zenodo. https://doi.org/10.5281/zenodo.15738654
- Schlund, M., Hassler, B., Lauer, A., Andela, B., Jöckel, P., Kazeroni, R., et al. (2023). Evaluation of native Earth system model output with ESMValTool v2.6.0. Geoscientific Model Development, 16(1), 315–333. https://doi.org/10.5194/gmd-16-315-2023
- Schneck, R., Gayler, V., Nabel, J. E. M. S., Raddatz, T., Reick, C. H., & Schnur, R. (2022). Assessment of JSBACHV4.30 as a land component of ICON-ESM-v1 in comparison to its predecessor JSBACHV3.2 of MPI-ESM1.2. *Geoscientific Model Development*, 15(22), 8581–8611. Retrieved from https://gmd.copernicus.org/articles/15/8581/2022/doi:10.5194/gmd-15-8581-2022
- Schulz, M., Textor, C., Kinne, S., Balkanski, Y., Bauer, S., Berntsen, T., et al. (2006). Radiative forcing by aerosols as derived from the aerocom present-day and pre-industrial simulations. *Atmospheric Chemistry and Physics*, 6(12), 5225–5246. https://doi.org/10.5194/acp-6-5225-2006
- Seifert, A., & Beheng, K. D. (2006). A two-moment cloud microphysics parameterization for mixed-phase clouds. Part 1: Model description. Meteorology and Atmospheric Physics, 92(1–2), 45–66. https://doi.org/10.1007/S00703-005-0112-4/METRICS
- Smith, C. J., Kramer, R. J., Myhre, G., Alterskjær, K., Collins, W., Sima, A., et al. (2020). Effective radiative forcing and adjustments in CMIP6 models. Atmospheric Chemistry and Physics, 20(16), 9591–9618. https://doi.org/10.5194/acp-20-9591-2020
- Smith, D. M., Screen, J. A., Deser, C., Cohen, J., Fyfe, J. C., García-Serrano, J., et al. (2019). The Polar Amplification Model Intercomparison Project (PAMIP) contribution to CMIP6: Investigating the causes and consequences of polar amplification. *Geoscientific Model Development*, 12(3), 1139–1164. https://doi.org/10.5194/gmd-12-1139-2019
- Sogacheva, L., Popp, T., Sayer, A. M., Dubovik, O., Garay, M. J., Heckel, A., et al. (2020). Merging regional and global aerosol optical depth records from major available satellite products. *Atmospheric Chemistry and Physics*, 20(4), 2031–2056. https://doi.org/10.5194/acp-20-2031-
- Stengel, M., Stapelberg, S., Sus, O., Finkensieper, S., Würzler, B., Philipp, D., et al. (2020). CLOUD_CCI advanced very high resolution radiometer post meridiem (AVHRR-PM) dataset version 3: 35-year climatology of global cloud and radiation properties. *Earth System Science Data*, 12(1), 41–60. https://doi.org/10.5194/essd-12-41-2020
- Stevens, B. (2015). Rethinking the lower bound on aerosol radiative forcing. *Journal of Climate*, 28(12), 4794–4819. https://doi.org/10.1175/ JCLI-D-14-00656.1
- Stevens, B., Fiedler, S., Kinne, S., Peters, K., Rast, S., Müsse, J., et al. (2017). MACv2-SP: A parameterization of anthropogenic aerosol optical properties and an associated Twomey effect for use in CMIP6. Geoscientific Model Development, 10(1), 433–452. https://doi.org/10.5194/gmd-10-433-2017
- Sundqvist, H., Berge, E., & Kristjánsson, J. E. (1989). Condensation and cloud parameterization studies with a mesoscale numerical weather prediction model. *Monthly Weather Review*, 117(8), 1641–1657. https://doi.org/10.1175/1520-0493(1989)117(1641:CACPSW)2.0.CO;2
- Taylor, K., Williamson, D., & Zwiers, F. (2000). The sea surface temperature and sea ice concentration boundary conditions for AMIP II simulations (Tech. Rep.). Lawrence Livermore National Laboratory. Retrieved from https://pcmdi.llnl.gov/report/pdf/60.pdf
- Taylor, K. E., Stouffer, R. J., & Meehl, G. A. (2012). An overview of CMIP5 and the experiment design. Bulletin of the American Meteorological Society, 93(4), 485–498. https://doi.org/10.1175/BAMS-D-11-00094.1
- Taylor, K., Williamson, D., & Zwiers, F. (2015). AMIP sea surface temperature and sea ice concentration boundary conditions (Tech. Rep.). Lawrence Livermore National Laboratory. Retrieved from https://pcmdi.llnl.gov/mips/amip/details/index.html
- Tselioudis, G., Rossow, W. B., Jakob, C., Remillard, J., Tropf, D., & Zhang, Y. (2021). Evaluation of clouds, radiation, and precipitation in CMIP6 models using global weather states derived from ISCCP-H cloud property data. *Journal of Climate*, 34(17), 7311–7324. https://doi.org/10.1175/JCLI-D-21-0076.1
- Twomey, S. (1974). Pollution and the planetary albedo. Atmospheric Environment, 8(12), 1251–1256. https://doi.org/10.1016/0004-6981(74) 90004-3
- van Vuuren, D., O'Neill, B., Tebaldi, C., Chini, L., Friedlingstein, P., Hasegawa, T., et al. (2025). The scenario model intercomparison project for CMIP7 (ScenarioMIP-CMIP7). EGUsphere, 2025, 1–38. https://doi.org/10.5194/egusphere-2024-3765
- Vignesh, P. P., Jiang, J. H., Kishore, P., Su, H., Smay, T., Brighton, N., & Velicogna, I. (2020). Assessment of CMIP6 cloud fraction and comparison with satellite observations. Earth and Space Science, 7(2), e2019EA000975. https://doi.org/10.1029/2019EA000975

FIEDLER ET AL. 21 of 22



Journal of Advances in Modeling Earth Systems

- 10.1029/2025MS005067
- Vogel, A., Alessa, G., Scheele, R., Weber, L., Dubovik, O., North, P., & Fiedler, S. (2022). Uncertainty in aerosol optical depth from modern aerosol-climate models, reanalyses, and satellite products. *Journal of Geophysical Research: Atmospheres*, 127(2), e2021JD035483. https://doi.org/10.1029/2021JD035483
- Wahl, S., & Fiedler, S. (2025). Validation of CMIP7 updated aerosol forcing with ICON-XPP. DOKU at DKRZ. Retrieved from https://www.wdc-climate.de/ui/entry?acronym=DKRZ/_LTA/_1198/_ds00004
- Wilcox, L. J., Allen, R. J., Samset, B. H., Bollasina, M. A., Griffiths, P. T., Keeble, J., et al. (2023). The Regional Aerosol Model Intercomparison Project (RAMIP). Geoscientific Model Development, 16(15), 4451–4479. https://doi.org/10.5194/gmd-16-4451-2023
- Williams, A. I. L., Stier, P., Dagan, G., & Watson-Parris, D. (2022). Strong control of effective radiative forcing by the spatial pattern of absorbing aerosol. *Nature Climate Change*, 12(8), 735–742. https://doi.org/10.1038/s41558-022-01415-4
- Winker, D. M., Pelon, J., Coakley, J. A., Ackerman, S. A., Charlson, R. J., Colarco, P. R., et al. (2010). The CALIPSO mission: A global 3D view of aerosols and clouds. *Bulletin of the American Meteorological Society*, 91(9), 1211–1230. https://doi.org/10.1175/2010BAMS3009.1
- Xian, P., Reid, J. S., Hyer, E. J., Sampson, C. R., Rubin, J. I., Ades, M., et al. (2019). Current state of the global operational aerosol multi-model ensemble: An update from the international cooperative for aerosol prediction (ICAP). *Quarterly Journal of the Royal Meteorological Society*, 145(S1), 176–209. https://doi.org/10.1002/qj.3497
- Zängl, G., Reinert, D., Rípodas, P., & Baldauf, M. (2015). The ICON (ICOsahedral Non-hydrostatic) modelling framework of DWD and MPI-M: Description of the non-hydrostatic dynamical core. *Quarterly Journal of the Royal Meteorological Society*, 141(687), 563–579. https://doi.org/10.1002/QJ.2378
- Zhang, Y., & Rossow, W. B. (2023). Global radiative flux profile data set: Revised and extended. *Journal of Geophysical Research: Atmospheres*, 128(5), e2022JD037340. https://doi.org/10.1029/2022jd037340
- Zhang, Y., & Steiner, A. L. (2022). Projected climate-driven changes in pollen emission season length and magnitude over the continental United States. *Nature Communications*, 13(1), 1234. https://doi.org/10.1038/s41467-022-28764-0

FIEDLER ET AL. 22 of 22